6.8.2 First Wall Protection System

6.8.2.1 Introduction and Overall Configuration – The first wall system surrounds the entire cavity chamber. It uses a SiC/SiC composite structural material and Pb coolant and film protectant. The cavity has a central cylindrical section and upper and lower end caps. The baseline design has a cylinder height equal to the radius. Longer cylinders were also considered, but rejected primarily due to their lower average power density.

As shown earlier in Figure 6.8-1, the Prometheus-L cavity is encircled and penetrated by 60 beamlines. Accommodation of these beams is a very challenging engineering problem, but the choice of a wetted wall makes the problem more tractable than with a thick liquid curtain.

The first wall system consists of a series of panels 2-m wide which are lowered into the cavity vertically. Figure 6.8.2-2 shows a cross sectional view of a first wall panel. The cooling channels are 5-cm thick to provide neutron multiplication needed for tritium breeding. The first wall is kept thin (5 mm) to provide good heat conduction into the coolant. The film thickness is also minimized for good heat transfer as well as to reduce the problem of liquid entering the cavity.

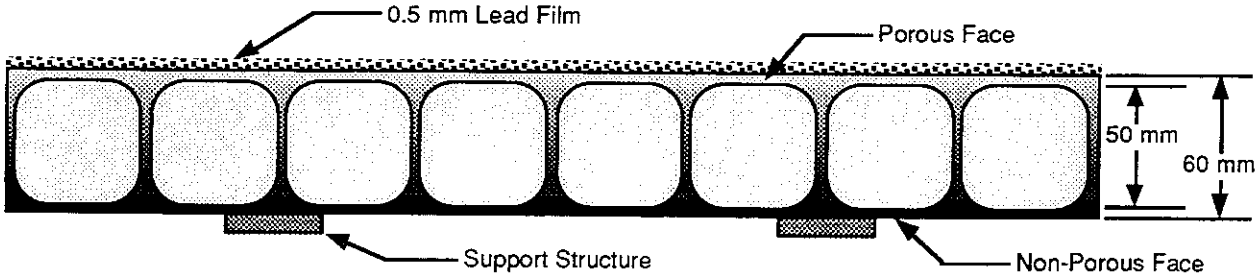

Figure 6.8.2-1 First Wall Panel; Cross Sectional View

The cooling system is separate from the blanket. The total amount of heat deposited in the first wall system is large (~1200 MW), requiring substantial flow of the Pb coolant. The large first wall system heating rate (as compared with MFE designs) is due in part to the conversion of neutron energy to x-ray and debris energy in the pellet and also the large amount of neutron power deposited in the thick Pb coolant. A more detailed description of the cooling system thermal hydraulics is found in Section 6.8.2.2.

Pb also acts as the first wall protectant. A film nominally 0.5 mm in thickness is allowed to form on the surface facing the pellet explosions. The porosity of the bulk

SiC is tailored to allow Pb from the cooling channels to slowly seep onto the surface. This surface film evaporates in response to the intense heat flux from the target explosions and then recondenses prior to the next shot. The energy deposition characteristics are central to several key responses in the cavity, including vapor dynamics, cavity clearing, and mechanical loading on the first wall system. Section 6.8.2.3 gives a detailed account of the x-ray and debris energy deposition. Nuclear heating is described in more detail in Section 6.8.1.

The behavior of the cavity vapor is very important in determining the loadings on the wall and the recondensation which is required for a high repetition rate. The actual behavior of the cavity vapor following an explosion is very complex, involving time-dependent non-linear processes. Two simplified analyses were performed to help provide insight into this complex behavior. Section 6.8.2.4 examines the vapor response using a 1-D time-dependent hydrodynamic model. These calculations provide the pressure and temperature histories at the wall and throughout the vapor.

In the Prometheus design, cavity clearing requires good conduction heat transfer into the cooling channels. Prometheus-L requires the cavity vapor to drop below 1 mtorr before the laser beams are fired, whereas Prometheus-H has a window of 10-100 mtorr. The lower limit is needed to establish proper channel transport conditions, and the upper limit is based on target injection constraints. Section 6.8.2.5 examines vapor clearing using a simplified (lumped parameter) model of vapor condensation, but more sophisticated modeling of the thermal responses. Adequate clearing times are predicted for both reactors.

Protection of the first structural wall is accomplished using a thin film which wets the surface. Wetting of SiC by Pb is assisted by coating the SiC with a metal as part of the CVD process. Protection of the upper end cap is a particularly difficult problem. In order to maintain a fully-wetted surface without Pb falling off into the cavity, we inject a thin Pb jet at the top of the upper end cap. The jet injector structure (SiC) is exposed to the blast effects and is made easily accessible for repair or replacement, as required. The fluid leaves the injector and flows along the surface. Figure 6.8.2-1 shows the overall configuration of the film flow system. Section 6.8.2.6 provides analysis of the film flow characteristics, including flow through porous structures and film flow along the wall.

The first wall system structural material is SiC/SiC composite. The material is woven from SiC fabric and then impregnated with SiC using a chemical vapor deposition (CVD) process. These panels are inserted and removed from the reactor vertically. They are structurally attached to the blanket through a locking mechanism described

in Section 6.11. The ability of these panels to withstand the cyclic loading from the blast is analyzed in Section 6.8.2.7.

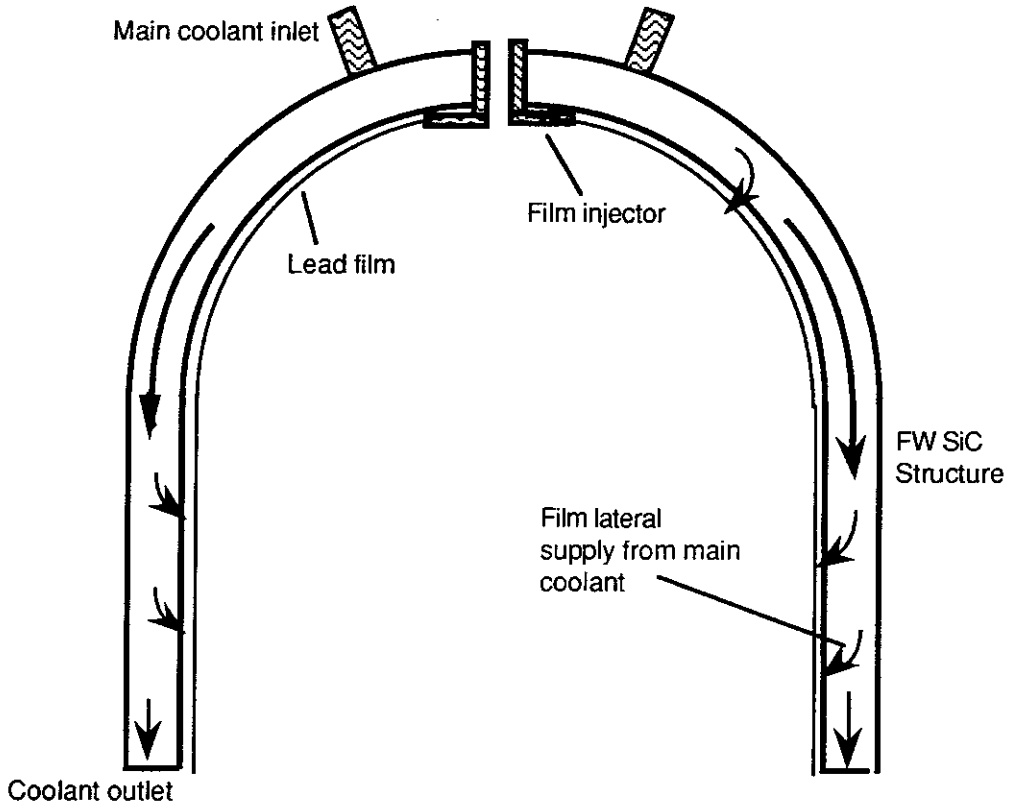

Figure 6.8.2-2 Schematic View of Film Supply Systems

The expected lifetime of the first wall panels has been estimated as five years. This is primarily due to radiation damage in the SiC and to surface damage and fatigue caused by pulsing.

Tables 6.8.2-1 and 6.8.1-2 summarize the major parameters of the first wall system. In the analysis that follows, some discrepancies may appear in the values used for the major system parameters. The final design point was determined after most of these more detailed analyses were completed.

Table 6.8.2-1 First Wall System Major Parameters

	Laser	HI	
First Wall Radius	5.0	4.5	m
Cylinder Height	5.0	4.5	m
Total Height	15	13.5	m
Surface Area	471	382	m^2
Volume	916	668	m^3
Film Thickness		0.4-0.6	mm
Cooling Channel Wall Thickness		5	mm
Cooling Channel Diameter		5	cm
Mean Fiber Pore Diameter		50	μm
Porosity		10	%
Permeability		1.76×10^{-14}	m^2
Pb Inlet/Outlet Temperature		375/525	°C
Inlet/Outlet Pressure		2.0/1.5	MPa
Pumping Power (In Reactor)		3-4	MW
Maximum SiC Temperature		775	°C

Table 6.8.2-2 First Wall Power Balance

	Laser	HI	
Total Yield	497	719	MJ
Neutron Yield	359	514	MJ
X-ray Yield	31	46	MJ
Debris Yield	107	159	MJ
Repetition Rate	5.6	3.5	Hz
Surface Power	780	725	MW
Nuclear Heating	488	437	MW
Total First Wall System Power	1268	1162	MW

6.8.2.2 Cooling System Thermal-Hydraulics - The cooling system is designed to provide the necessary flow conditions to maintain all components within allowable temperature and pressure limits. A summary of values of the thermal hydraulic parameters and heat transfer properties used in this study is given in Table 6.8.2-3. More details on the film thermal hydraulics can be found in Sections 6.8.2.5 and 6.8.2.6.

The Pb bulk temperature rise in the main coolant is maximized in order to reduce the flow rate. The Pb must be kept well above the melting point (327°C) but low enough to avoid compatibility limits with steel in the heat transport loop. This led to inlet and outlet temperatures of 375° and 525°C.

The first wall power comes from both surface heating (from x-rays and debris) and nuclear heating. The lead flow rate needed to remove the first wall thermal power is estimated using:

$$\dot{m}\, C_p\, \Delta T = \dot{Q}_{fw} \qquad (6.8.2\text{-}1)$$

Where $\dot{m}$ is the mass flow rate and $\dot{Q}_{fw}$ is the power to the first wall. The lead velocity in the vertical side of the chamber is determined from the total flow area:

$$A \cdot V = \dot{m} \qquad (6.8.2\text{-}2)$$

The frictional pressure drop is calculated as:

$$\Delta P = f \frac{\rho V^2 L}{2 D_h} \qquad (6.8.2\text{-}3)$$

where f is the friction factor obtained from the Moody diagram using a relative roughness of 0.001. L is the coolant flow path length and D_h is the equivalent diameter. The pumping power for the cavity chamber is the product of the pressure loss in the chamber times the volumetric flow rate:

$$P\rho = \frac{m\, \Delta P}{\rho \eta} \qquad (6.8.2\text{-}4)$$

Table 6.8.2-3 First Wall System Thermal Hydraulic Parameters

	Prometheus-L	Prometheus-H	Units
Fusion Thermal Power	3092	2797	MW
Total FW Thermal Power	1268	1162	MW
Coolant	Pb	Pb	
Impurities	Bi, Sb, W	Bi, Sb, W	
Film Thickness	0.4 – 0.6	0.4 – 0.6	mm
Cooling Channel Diameter	5	5	cm
Inlet Bulk Temperature	375	375	℃
Outlet Bulk Temperature	525	525	℃
ΔT_{bulk}	150	150	℃
Mass Flow Rate	58,770	54,422	kg/s
Volume Flow Rate	5.65	5.21	m^3/s
Coolant Flow Area (vertical side of chamber)	1.1775	1.1775	m^2
Average Velocity	4.8	4.42	m/s
Reynolds Number	$1.2x10^6$	$1.12x10^6$	
Frictional Factor	0.02	0.02	
Coolant Path	12.85	12.34	m
Frictional Pressure Drop	0.615	0.5	MPa
Inlet Pressure (top)	1.0	1.0	MPa
Outlet Pressure (bottom)	1.385	1.5	MPa
Pumping Power (85% efficiency)	4.1	3.0	MW
Properties			
c_p (Pb)	154		J/kg-K
ρ (Pb)	10400		kg/m^3
μ (Pb)	$2.059x10^{-3}$		$N-s/m^2$
k (Pb)	34		W/m-K
T_{mp} (Pb)	327		℃
hfg	862,500		J/kg

6.8.2.3 X-ray and Debris Spectra and Energy Deposition – Energy deposition from the blast is estimated by calculating the attenuation of x-rays and debris in the cavity vapor and deposition profiles in the film. The x-rays reach the wall in ~20 ns—prior to the debris ions—and cause substantial evaporation of the Pb protective film. Debris energy then deposits primarily in the cavity vapor. Depending on the yield, spectra, and attenuation coefficients in the liquid film, some amount of liquid is raised beyond the boiling point and is immediately vaporized. Additional liquid is vaporized by intense thermal radiation from the hot cavity gas. (We call this latter process "secondary evaporation".) In this subsection, calculations are described for:

(1) X-ray energy deposition in the cavity vapor
(2) X-ray deposition profile of the lead film and vaporization depth
(3) Debris energy deposition in the cavity vapor
(4) Reactive impulse due to the vaporized gas.

Secondary evaporation is covered in more detail in Section 6.8.2.5.

For this analysis, the x-ray spectra of SIRIUS[1] and LIBRA[2,3] were used for the KrF and heavy ion designs, respectively (see Figure 6.8.2-3). Other base case chamber parameters used for these calculations are shown in Table 6.8.2-4.

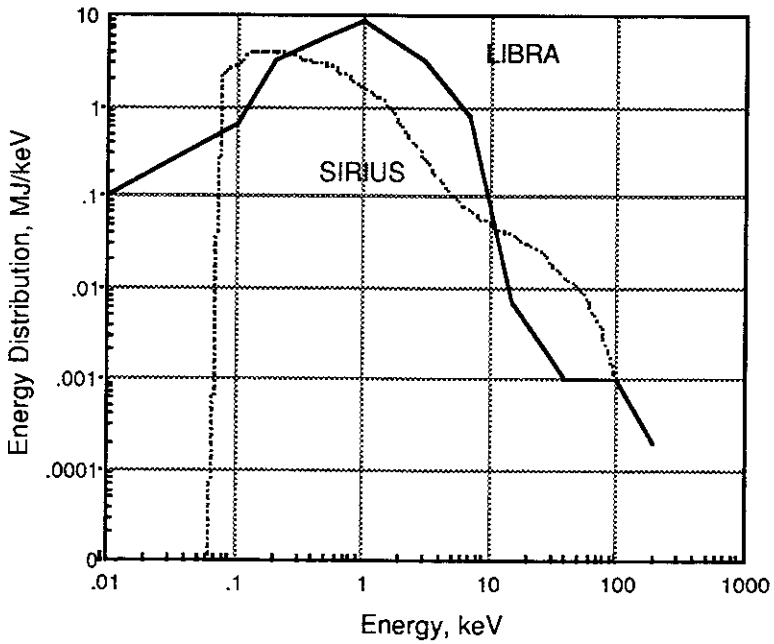

Figure 6.8.2-3 Target X-ray Spectra Used for Prometheus-L (SIRIUS) and -H (LIBRA)

Table 6.8.2-4 Chamber Parameters (Base Cases)

	Laser	HI	Units
Pressure Limit @ 0°C	0.001	0.1	torr
Background Gas Density	3.5×10^{13}	3.5×10^{15}	cm^{-3}
Total Yield	497	719	MJ
Neutron Yield	359	514	MJ
X-ray Yield	31	46	MJ
Debris Ion Yield	107	159	MJ
Cavity Radius	5.0	4.5	m
Cavity Height	15	13.5	m
First Wall Area	471.2	381.7	m^2
Cavity Volume	916.2	668.0	m^3

X-Ray Absorption in the Cavity Vapor – As the x-rays travel toward the wall, some are absorbed by the background gas. The attenuation of x-rays is exponential. At low energies, this process is dominated by the photoelectric interaction. In this process, electrons are ejected from the Pb atoms. (We assume for this calculation that the cavity gas contains only Pb.) When the vacancies are refilled, additional x-rays may be emitted; however, their energy will be substantially lower where the absorption cross section is very high. Most of the energy is ultimately transformed into kinetic energy of the gas. The attenuation cross section in lead is shown in Figure 6.8.2-4. [4] Note how strongly dependent it is on energy.

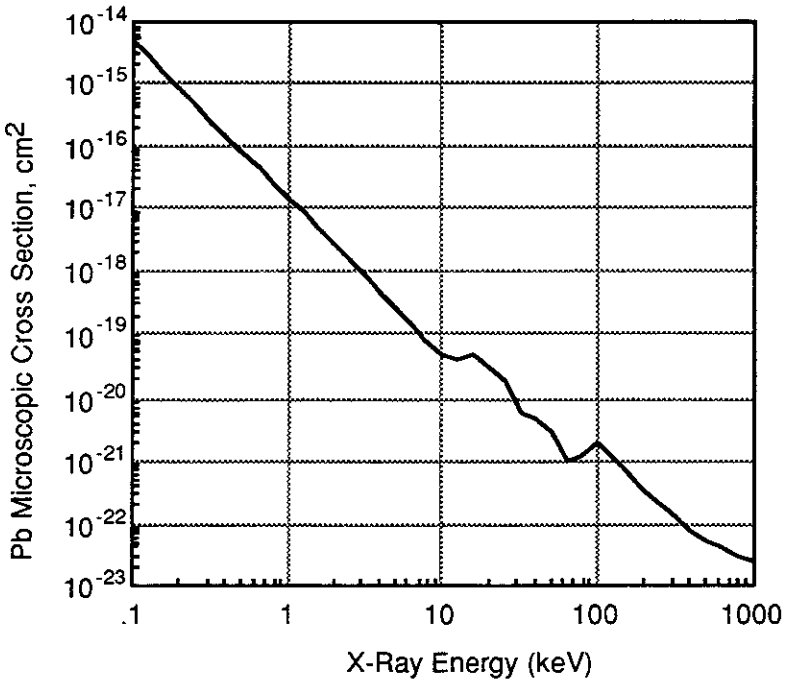

Figure 6.8.2-4 Cross-Section in Pb as a Function of X-Ray Energy

The equations used to calculate the x-ray energy attenuation in the cavity vapor are:

$$E_{dep} = 4\pi \int_0^r r^2 \sum_{i=1}^{n} q_i \, d\,r \qquad [J] \qquad (6.8.2\text{-}5)$$

$$q_i = \mu_{iv} \frac{E_i}{4\pi r^2} e^{-\mu_{iv} r} \qquad [J/m^3] \qquad (6.8.2\text{-}6)$$

where E_{dep} is the energy deposited within a depth r, q_i is the volumetric energy deposition at r for the i^{th} x-ray energy group, E_i is the total energy in group i (in Joules), and μ_{iv} is the macroscopic absorption cross section in the vapor (at a given pressure) for energy group i. These equations were solved and then normalized to the initial x-ray yield.

The fraction of x-rays absorbed as a function of radius for the laser and heavy ion reactors is shown in Figure 6.8.2-5. The heavy ion cavity absorbs a much larger amount of energy due to its higher base pressure (100 mtorr vs. 1 mtorr). The remainder of the energy is absorbed in the film.

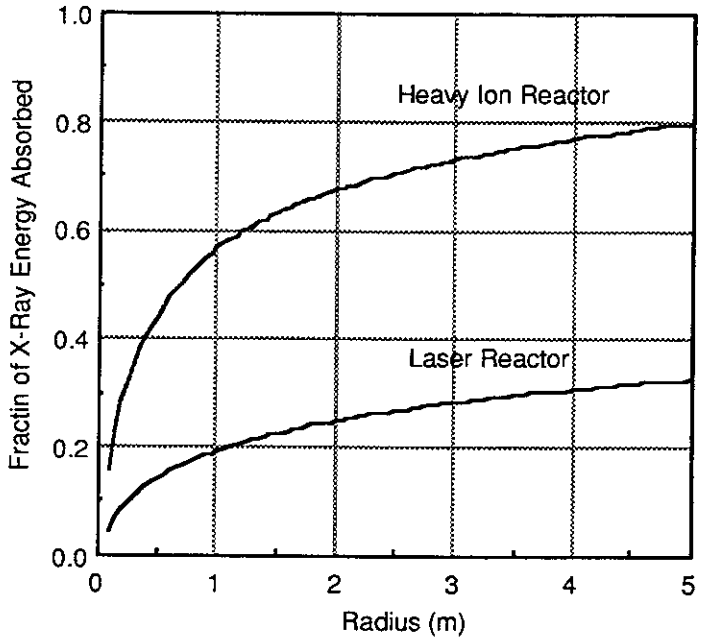

Figure 6.8.2-5 Fraction of X-ray Energy Absorbed by the Lead Vapor.

Energy Deposition and Evaporation of the Film – Similar equations can be used in the film region to find the approximate depth of evaporation that is caused by the x-rays. The geometry in this case is linear, rather than cylindrical, leading to the following equations:

$$E_{dep} = 4\pi R^2 \int_0^x \sum_{i=1}^{n} q_i \, dx \qquad [J] \qquad (6.8.2\text{-}7)$$

$$q_i = \mu_{if} F_i e^{-\mu_{if} x} \qquad [J/m^3] \qquad (6.8.2\text{-}8)$$

$$F_i = \frac{E_i}{4\pi R^2} e^{-\mu_{iv} R} \qquad [J/m^2] \qquad (6.8.2\text{-}9)$$

where F_i is the x-ray energy flux incident on the wall, R is the radius of the wall, x is the depth into the film, and μ_{if} is the macroscopic absorption cross section of the film. Figure 6.8.2-6 shows the resulting energy deposition profiles for both the laser and heavy ion cases.

The energy per unit volume required to raise the lead to its boiling point is given by:

$$E_{bp} = C_p (T_{sat} - T_{surface}) \qquad (6.8.2\text{-}10)$$

and the energy required to evaporate is given by:

$$E_{vap} = h_v + C_p (T_{sat} - T_{surface}) \qquad (6.8.2\text{-}11)$$

where

h_v	= 862,500 J/kg	heat of evaporation per unit volume
C_p	= 154 J/kg-°K	heat capacity
T_{sat}	= ~1500 °K	(saturation temperature following the blast)
$T_{surface}$	= 950-1150 °K	(surface temperature preceding the blast)
E_{bp}	~ 54-85 x 10^3 J/kg	
E_{vap}	~ 10^6 J/kg	

The depth corresponding to E_{bp} is called X_{bp} and the depth corresponding to E_{vap} is called X_{vap}. In the region between these two depths, the lead will be in a two-phase state. This is modeled by assuming some additional vaporization. The additional thickness (X_{tot}–X_{vap}) of the vaporized layer beyond X_{vap} is computed by integrating the energy deposited in the two-phase region and determining the amount of mass this energy would evaporate:

$$X_{tot} - X_{vap} = \frac{\int_{X_{vap}}^{X_{bp}} (q - C_p \Delta T)\, dX}{h_{fg}} \qquad (6.8.2\text{-}12)$$

Figure 6.8.2-7 is a plot of the integral of the deposition profile – $\int q\, dX$. This is used in Eq. 6.8.2-12 to obtain the net depth of evaporation. The mass of vaporized lead then can be calculated simply as:

$$M = \rho\, 4\pi R^2\, X_{tot} \qquad (6.8.2\text{-}13)$$

Table 6.8.2-5 summarizes the results. Note, the total mass evaporated during a pulse is much larger than shown in the table because thermal radiation was not considered here. These results represent only the initial evaporation from x-rays. Section 6.8.2.5 provides more information on the effects of thermal radiation.

Table 6.8.2-5 Mass and Thickness of Layer Vaporized by X-Rays

	Laser	HI	
X-ray Energy Absorbed in Vapor	9.9	28.9	MJ
X-ray Energy Deposited in Film	21.1	8.1	MJ
X_{vap}	0.6	0.5	μm
X_{bp}	5.5	5.9	μm
Vaporized Film Thickness, X_{tot}	1.3	1.6	μm
Surface Area	471	382	m2
Vaporized Mass	5.9	6.4	kg

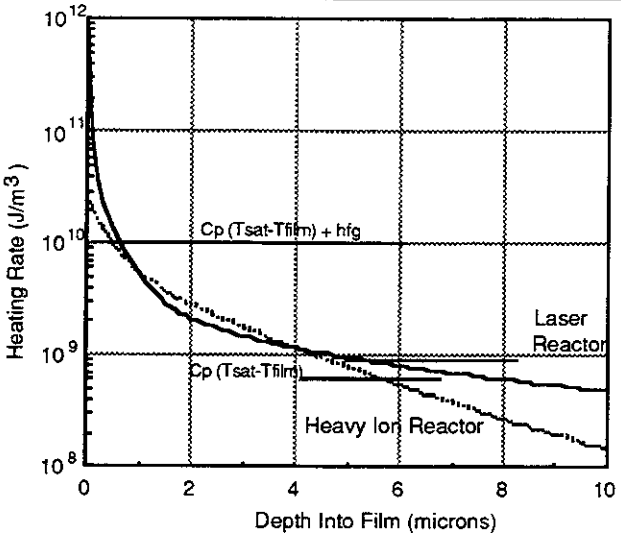

Figure 6.8.2-6 Energy Deposition Profile in Pb Film

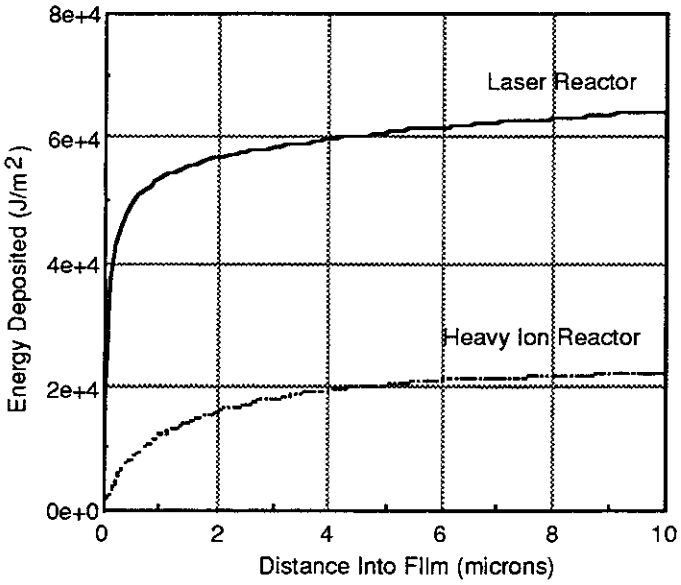

Figure 6.8.2-7 Integrated Energy Deposition Profile in Pb Film

Debris Energy Deposition – Debris energy deposition into the cavity gas was calculated using the methods in References 5 and 6. The debris spectra were estimated by assuming the ions are all ejected at the same velocity.[1] If all ions have the same velocity, then the debris yield (E) is given by:

$$E = \frac{1}{2} M v^2 \qquad (6.8.2\text{-}14)$$

$$M = (M_D + M_T + M_{He} + M_C + M_H + M_{Pb}) \qquad (6.8.2\text{-}15)$$

where M_i represents the total mass of debris species i. If m_i is the mass of a single ion and e is the energy per ion, then:

$$e = \frac{1}{2} m_i v^2 = \frac{E m_i}{M} \qquad (6.8.2\text{-}16)$$

Table 6.8.2-6 lists the debris types, their masses, and energies. The mass of He is computed assuming a burn fraction of 30%.

Using these values, the fraction of debris energy absorbed in the cavity was calculated and is shown in Figure 6.8.2-8. For the heavy ion reactor conditions (assuming 100 mtorr), essentially all of the debris is stopped by the cavity vapor. For the laser

Table 6.8.2-6 Target Debris Ion Spectra and Masses

Laser				HI		
Ion	e (keV)	Mass (mg)	No. of Ions	e (keV)	Mass (mg)	No. of Ions
D	30.57	1.33	4.01×10^{20}			
T	45.85	2.0	4.01×10^{20}	Similar data can be generated for		
He	41.45	1.14	1.72×10^{20}	the Heavy Ion Option Target Debris		
C	183.59	16.27	8.16×10^{20}			
H	15.3	1.36	8.16×10^{20}			
Pb	0	0	0			

case (1 mtorr), 20% of the debris energy reaches the wall. However, since the debris travels much slower than the x-rays, by the time the ions approach the film, the density of the evaporated lead vapor is so high that it can be assumed that the debris will lose all its energy before reaching the liquid layer.

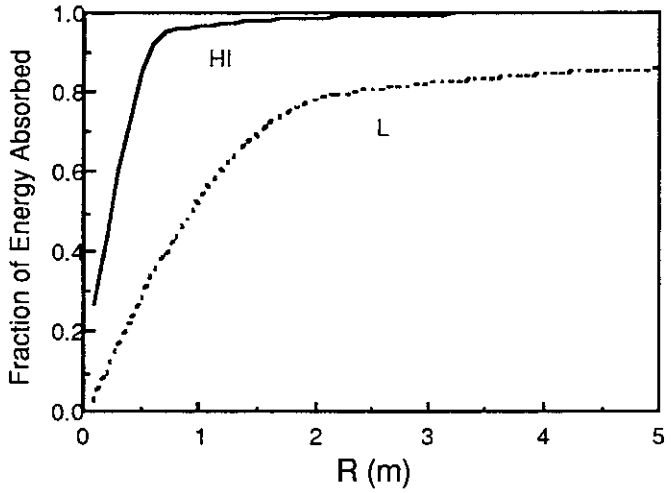

Figure 6.8.2-8 Debris Ion Deposition Profiles in Cavity Vapor

Impulse Due to Vaporized Gas – The reactive impulse of vaporized gas is estimated as $M_{gas}V$, where V is the average gas velocity. The average gas velocity can be estimated using the bulk kinetic energy of the vaporized fluid, which is equal to the deposited x-ray energy less the energies of ionization, vaporization, and dissipation in the film.

$$E_{kinetic} = f_{wall} E_{yield} - E_{vaporization} - E_{ionization} - E_{dissipation\ in\ film} \qquad (6.8.2\text{-}17)$$

$$= \frac{M_{gas} V^2}{2} \qquad (6.8.2\text{-}18)$$

$$\Delta I_{x\text{-}ray} = M_{gas} V \qquad (6.8.2\text{-}19)$$

To estimate the energy of ionization, we need to know the amount of gas ionized. The fraction of the gas ionized can be determined by the Saha equation, which is written as:

$$f = \frac{N_i}{N_o} = \left(2.4 \times 10^{15} \frac{T^{3/2}}{N_o} e^{(-U_i/kT)} \right)^{0.5} \qquad (6.8.2\text{-}20)$$

The fraction of the gas ionized at a gas temperature of 7 eV (81,200 K) is about 18% and decreases to 0.21% at a gas temperature of 1 eV. For Prometheus-L, the vaporized gas temperature is about 5000 K, as estimated from the equation of state. Then the amount of ionized gas is small and can be neglected. For this case, the reactive impulse due to x-ray vaporized gas is 10,400 N-s. This is relatively small, indicating that the mechanical responses in the structures should be manageable. The reactive impulse due to x-ray vaporized gas for the Prometheus-H is negligible due to the gas having a small amount of kinetic energy.

References for 6.8.2.3

1. B. Badger, et al., "SIRIUS-T: A Study of a Symmetrically-Illuminated Inertial Confinement Fusion Tritium Production Facility Final Report" UWFDM-850, December 1990.

2. M. E. Sawan, et al., "Chamber Design for the LIBRA Light Ion Beam Fusion Reactor," Fusion Technology, Vol.15, No. 2, Part 2A, p. 766, March 1989.

3. G. A. Moses, et al., "Overview of LIBRA Light Ion Beam Fusion Conceptual Design", Fusion Technology, Vol. 15, No. 2, Part 2A, 756 (1989).

4. F. H. Attix and W. C. Roesch, "Radiation Dosimetry; Volume I Fundamentals," Academic Press, New York, p. 119, 1968.

5. H. H. Anderson and J. F. Ziegler, Hydrogen Stopping Powers and Ranges in All Elements", Pergammon Press (1977).

6. J. F. Ziegler, Helium Stopping Powers and Ranges in All Elements, Pergammon Press (1977).

6.8.2.4 Cavity Hydrodynamics – It has been shown in the previous section that energy deposition of x-rays and ion debris in the lead film leads to evaporation, subsequent energy absorption in the evaporated lead, and energy re-radiation. A complete and accurate description of the hydrodynamics of these processes is essential in two respects:

(1) The re-condensation rate of Pb vapor is sensitively dependent on the exact temperature and pressure conditions at recondensation surfaces. Hence, the frequency of microexplosions is highly dependent on detailed hydrodynamical calculations.
(2) The mechanical response of the SiC structure is dictated by the magnitude and duration of the Pb vapor pressure at the surface. It is also depedent on the reactive impulse due to vaporized Pb.

Hydrodynamical modeling of the Pb vapor, including space-time energy deposition in the Pb vapor, gas ionization, and coupled radiation transport is obviously complicated and requires extensive resources. However, the fundamental hydrodynamical behavior of the system can be studied if a number of approximations are made. These are:

(1) The fluid equations are solved in one-dimensional cylindrical geometry (i.e., ignoring effects of end caps).
(2) Coupled particle and photon transport is approximated by a lumped model, where the total energy deposited in the vapor by x-rays and ion debris is delivered to the lead film as Q"(t).

These simplifying assumptions render the hydrodynamical model greater simplicity, as described in the next sections. We will first state the problem and follow this by a description of the governing fluid equations. The numerical scheme developed for the solution of the fluid equations is then presented. Results are finally given in the last section.

Problem Statement – The evaporation and condensation processes are analyzed using a one-dimensional (1-D) hydrodynamic model of the vapor flow in the cavity as shown in Figure 6.8.2-9.

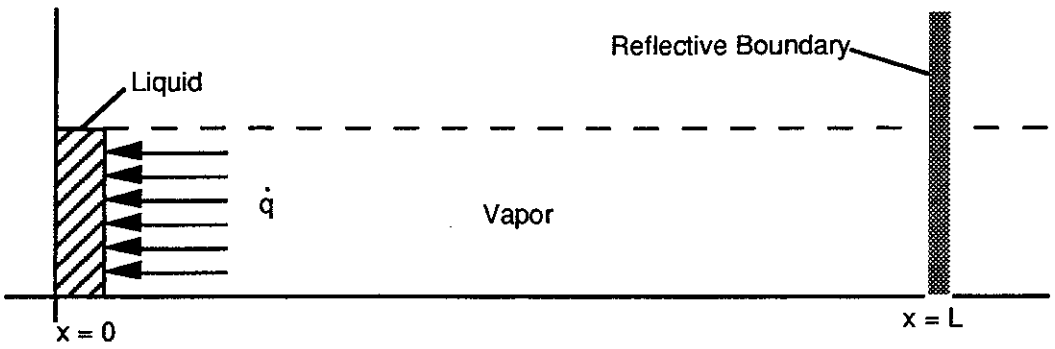

Figure 6.8.2-9 Mathematical Model of the Vapor Flow in the Cavity

Governing Equations – The governing equations are the time-dependent continuity, momentum, and energy equations of compressible fluid flow. An equation of state relates the pressure to the temperature and density. These equations in normalized, one-dimensional (1-D) form are:

$$\frac{\partial \rho}{\partial T} + \frac{\partial \rho u}{\partial x} = 0, \tag{6.8.2-21}$$

$$\frac{\partial \rho T}{\partial \tau} + \frac{\partial \rho u u}{\partial x} = \frac{\partial p}{\partial x} + \frac{\partial}{\partial x}\left(\frac{1}{Re}\frac{\partial u}{\partial x}\right) \tag{6.8.2-22}$$

$$\frac{\partial \rho T}{\partial t} + \frac{\partial \rho u T}{\partial x} = \frac{\partial}{\partial x}\left(\frac{1}{RePr}\frac{\partial T}{\partial x}\right) \tag{6.8.2-23}$$

$$p = \rho T \tag{6.8.2-24}$$

and are solved on the domain $(x, t) \in (0, L) \times (0, t_f)$. In these equations, ρ is density, u is velocity, T is temperature, and p is pressure in nondimensional form. The nondimensional parameters are Reynolds number, Re, and Prandtl number, Pr, defined as:

$$Re = \frac{\rho u_o D}{\mu}$$

$$Pr = \frac{\mu C_p}{k} \tag{6.8.2-25}$$

where ρu_o is the inlet mass flux at x=0, t=0; μ is dynamic viscosity; k is thermal conductivity; C_p is specific heat; and D is the cavity diameter.

Initial and Boundary Conditions - The pressure in the cavity is assumed initially to be very low, p_o (1 mTorr for the KrF laser systems and 100 m Torr for the HI system). Furthermore, there is no input heat and the stagnant vapor is in thermodynamic equilibrium with the wall-protecting liquid. The initial conditions are, therefore, formulated as:

$$\rho(x,0) = 1$$

$$\rho u(x,0) = 1 \qquad (6.8.2\text{-}26)$$

$$T(x,0) = T_{sat}(p_o)$$

The mass flux at the liquid-vapor interface is determined by equating the energy flux absorbed in the liquid layer (or the heat flux conducted out in the condensation process) to the evaporation (or condensation) rate times the latent heat of evaporation. The vapor temperature and density at the interface are assumed to have the saturation value according to the interface pressure. The boundary conditions are, therefore, formulated as:

$$\rho(0,t) = \rho_{sat}(p)$$

$$\rho u(0,t) = \frac{\dot{q}}{h_{fg}(T)} \qquad (6.8.2\text{-}27)$$

$$T(0,t) = T_{sat}(p)$$

where $\dot{q}$ has different values in the evaporation or condensation process. In the evaporation process,

$$\dot{q} = \frac{Q}{A\,\Delta t}$$

where Q is the total heat absorbed by the Pb in the cavity, A is the surface area, and Δt is a characteristic absorption time. In the condensation process,

$$\dot{q} = \frac{-k_{eff}}{\delta_{eff}}(T - T_w)$$

where k_{eff} and δ_{eff} are the effective conductivity and thickness of the wall and the protecting liquid. T_w is the outside temperature of the wall.

At the centerline of the cavity, the symmetry conditions are applied; that is,

$$\frac{\partial \rho\,(L,t)}{\partial x} = 0$$

$$\rho u(L,t) = 0 \qquad (6.8.2\text{-}28)$$

$$\frac{\partial T\,(L,t)}{\partial x} = 0$$

Here the subscript "sat" denotes properties of the vapor under saturation conditions.

Numerical Solution – The governing Eqs. 6.8.2-21 through 6.8.2-23 are solved for ρ, ρu, and T, respectively, with p recovered from the equation of state Eq. 6.8.2-24. For the sake of analysis, the nonlinear partial differential equations are cast in the general form:

$$\frac{\partial \Phi}{\partial t} + \frac{\partial}{\partial x}\left(u\Phi - \Gamma \frac{\partial \Phi/\rho}{\partial x}\right) = S \qquad (6.8.2\text{-}29)$$

This equation is discretized on the staggered grid shown in Figure 6.8.2-10. The temperature, density, and pressure are calculated at points indexed by i and the mass flux, ρu, is calculated at points indexed by ij where j = i +1/2.

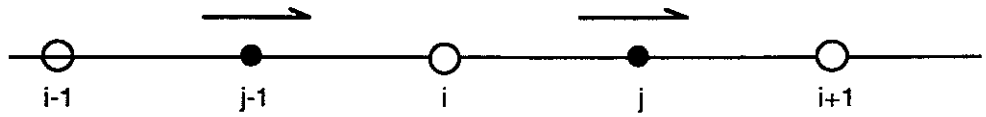

Figure 6.8.2-10. The Staggered Grid and Nodes

Using the backward Euler algorithm for time differencing and centered differences in space, Eq. 6.8.2-29 is approximated by:

$$-a_{1,i}\,\Phi_{i-1} + a_{2,i}\,\Phi_i - a_{3,i}\,\Phi_{i+1} = b_i \qquad (6.8.2\text{-}30)$$

where

$$a_{1,i} = D_{j-1}\,(1 + 1/2\ Pe_{j-1}), \qquad (6.8.2\text{-}31a)$$

$$a_{3,i} = D_j\,(1 - 1/2\ Pe_{j-1}), \qquad (6.8.2\text{-}31b)$$

$$a_{2,i} = a_{1,i} + a_{3,i} + (u_j - u_{j-1}) + \Delta x/\Delta t, \qquad (6.8.2\text{-}31c)$$

$$b_i = \Delta x\, S_i + \left(\frac{\Delta x}{\Delta t}\right)\Phi_i^n, \qquad (6.8.2\text{-}31d)$$

with

$$D_{j-1} = \frac{\Gamma_{j-1}}{\rho_{i-1}\,\Delta x},\quad D_1 = \frac{\Gamma_j}{\rho_{i+1}\,\Delta x},\quad Pe_1 = \frac{u_j\,\Delta x}{D_j}.$$

For stability and a unique solution, the coefficients of Eq. 6.8.2-30 should be positive. If the grid Peclet number, Pe_i is greater than two in magnitude, some of the coefficients defined by Eqs. 6.8.2-31 are not positive.

The governing equations generalized in Eq. 6.8.2-29 are nonlinear and coupled. Therefore, the coefficients of the difference equation, Eq. 6.8.2-30 are not constant. Block Gauss-Seidel method was used to solve Eqs. 6.8.2-21 through 6.8.2-23 for ρ, ρu, and T, successively. The coefficients were then evaluated using the data of the most recent iteration. The resulting linear systems were then solved by standard linear algebra methods. Iteration on the equations was stopped after convergence of all variables.

Standard Schemes - The coefficients of Eq. 6.8.2-30 are written in a general form as:

$$a_{1,i} = D_{j-1}\,A(Pe_{j-1}) + \max(0,u_{j-1}), \qquad (6.8.2\text{-}32a)$$

$$a_{3,i} = D_j\,A(Pe_j) + \max(0,-u_j), \qquad (6.8.2\text{-}32b)$$

$$a_{2,i} = a_{1,i} + a_{3,i} + (u_j - u_{j-1}) + \Delta x/\Delta t, \qquad (6.8.2\text{-}32c)$$

Expressions for A(Pe) for different schemes are listed in Table 6.8.2-7. Derivation of A(Pe) for first-order upwinding and power-law schemes can be found in Patankar[1] and for the CONDIF scheme in Runchal.[2] The parameter R appearing in Table 6.8.2-7 for the CONDIF scheme is defined as:

$$R = \frac{\Phi_{i-1} - \Phi_i}{\Phi_i - \Phi_{i-1}} \qquad (6.8.2\text{-}33)$$

It is clear, as discussed in Reference 2, that this provides a means of locating local extrema in the grid function Φ_i. If there is a sharp variation in Φ, then R may be quite large and, conversely, if there is only a small variation in Φ, R will be small. Therefore, a limit is imposed on R so that:

$$1/R_{max} \le R \le R_{max} \qquad (6.8.2\text{-}34)$$

Table 6.8.2-7 The Function A(Pe) for Different Schemes

Scheme	A(Pe)
CDS	$1.05\|Pe\|$
Upwinding	1
Power law	$\max[0,(1-0.1\|Pe\|)^5]$
CONDIF	$A(Pe_{j-1}) = 1 - \max(0,Pe_{j-1}/2) + R\max(0, Pe_j/2)$
	$A(Pe_j) = 1 - \max(0,Pe_j/2) + \frac{1}{R}\max(0, Pe_{j-1}/2)$

It can be seen, using the appropriate formulas from Table 6.8.2-7, that R_{max} controls the amount of numerical diffusion in the scheme. In particular, large values of R result in significant numerical diffusion while small values cause little diffusion. As noted in Reference 2, typical values are in the range $4 \leq R_{max} \leq 10$.

Filtering - Engquist, et al.[3] introduced nonlinear filters for shock computation. These filters are used as post-processors in conjunction with standard finite difference schemes. The difference equations are solved at the current time level, then the solutions are processed with the filter to eliminate oscillations before proceeding to the next time level. The filters control the total variation (i.e., they possess the TVD property), produce sharp shocks (they are second order away from shocks), and they are simple to use.

For the calculations reported herein, we use CDS and a nonlinear filter, as described below (for details, see Reference 3). The principles of the filtering technique are illustrated below using Fig. 6.8.2-11. Figure 6.8.2-11(a) shows the solution Φ^n at time t^n. Using Central Differential Scheme (CDS), the typical solution at time t^{n+1}, φ^{n+1}, is shown in Figure 6.8.2-11(b). This solution exhibits an overshoot, as would be expected. Results of filtering are displayed in Figure 6.8.2-11(c) where it can be seen that the overshoot has been completely removed. The basic principles of the filtering process are the following:

(1) $\varphi_{i_o}^{n+1}$ is detected as an overshoot via the test $\left(\Delta_-\varphi_{i_o}^{n+1}\right)\bullet\left(\Delta_+\varphi_{i_o}^{n+1}\right) < 0$.

(2) $\varphi_{i_o}^{n+1}$ is decreased in such a way that the new value of $\varphi_{i_o}^{n+1}$ is not less than $\varphi_{i_o-1}^{n+1}$

(3) $\varphi_{i_o+1}^{n+1}$ is increased by the same amount as $\varphi_{i_o}^{n+1}$ is decreased in order to maintain conservation properties and, thus, to obtain the right shock speed.

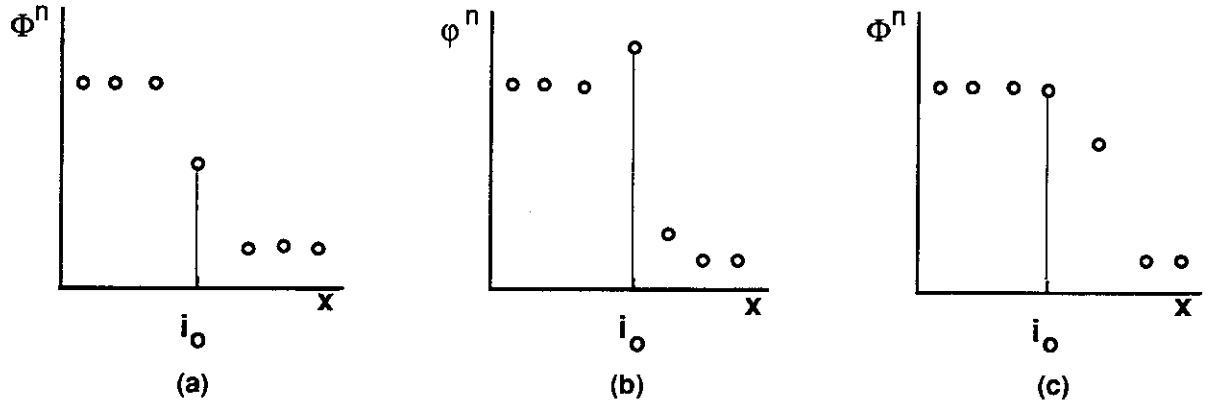

Figure 6.8.2-11 Filtering Process Applied to the CDS Result

The symbols Δ_- and Δ_+ denote the backward and forward differences, respectively, and are defined as $\Delta_\pm \Phi_i = \pm (\Phi_{i\pm1} - \Phi_i)$. It is of interest to note that the test used to detect overshoots is quite similar to that employed in CONDIF (Eq. 6.8.2-33), but subsequent steps of the algorithm are very different.

The algorithm for this filtering and also for more complicated ones, can be found in Reference 3, in which the nonlinearity and TVD properties of the filtering technique have been shown. We should emphasize that the above basic three-step process is not TVD, but the modifications needed (discussed in detail in Reference 3) are straightforward.

Input Heat - The calculations are carried out for two different working liquids: lithium and lead. The thermal properties of these liquids are listed in Table 6.8.2-8 which were obtained from Reference 4.

The total heat, Q, released in the case with lithium as working fluid is 100 MJ. The heat was assumed to be absorbed in the liquid layer in 10^{-6} seconds. Therefore, the input heat flux $\dot{Q} = 10^{14}$W, and the input heat flux per unit area $\dot{q} = 6.37 \times 10^{11}$W/m^2. The effective total area is $A_{eff} = 157$ m^2; that is,

$$q(t) = 6.37 \times 10^{11} \text{ W/m}^2 \qquad 0 < t \leq 10^{-6} \text{ s}$$

$$q(t) = 0 \qquad t > 10^{-6} \text{ s}$$

For the case with lead as working fluid, the released heat is in two parts: $Q_1 = 39.2$ MJ at time, $t = 10^{-8}$ s, and $Q_2 = 137.3$ MJ at time $t = 10^{-6}$. For the same effective area as

Table 6.8.2-8 Properties of Liquids Used in Hydrodynamics Calculations

Lithium		
Thermal Conductivity	liquid	$k = 48.4$ W/m-K
	vapor	$k = 0.04$ W/m-K
	effective	$k_{eff} = 23.15$ W/m-K
Specific Heat		$c_p = 4.17$ kJ/kg-K
Viscosity	vapor	$\mu = 7.6 \times 10^{-6}$ N-s/m^2
Latent Heat of Vaporization		$h_{fg} = 19.6$ MJ/kg
Effective Liquid Thickness		$\delta_{eff} = 1.5$ cm
Saturation Temperature		$T(K) = 7877.9/(4.8831 - \log_{10} p)$
Lead		
Thermal Conductivity	vapor	$k = 6.884 \times 10^{-4}\ \Omega \sqrt{T}$ W/m.K
	effective	$k_{eff} = 20.0$ W/m.K
Specific Heat		$c_p = 139.0$ J/kg.K
Viscosity	vapor	$\mu = 4.575 \times 10^{-6}\ \Omega \sqrt{T}$ N.s/m^2
Latent Heat of Vaporization		$h_{fg} = 0.85$ MJ/kg
Effective Liquid Thickness		$\delta_{eff} = 5.0$ cm
Saturation Temperature		$T(K) = 11290.0/(11.34 - \log_{10} p)$

Where, Ω is a function of temperature and is tabulated below.

T(K)	255.3	340.4	425.5	510.6	595.7	680.8	765.9	851.0	1702.
Ω	0.359	0.401	0.443	0.484	0.524	0.562	0.597	0.630	0.851

used for lithium, the first heat release is assumed to be absorbed in the liquid layer in 10^{-8} seconds and the second heat release in 10^{-6} seconds. Therefore,

$$\dot{q}(t) = 2.50 \times 10^{13} \text{ W/m}^2 \qquad 0 < t \leq 10^{-8} \text{ s}$$

$$\dot{q}(t) = 8.745 \times 10^{11} \text{ W/m}^2 \qquad 10\text{-}8 < t \leq 10^{-6} \text{ s}$$

$$\dot{q}(t) = 0 \qquad t > 10^{-6} \text{ s}$$

Results and Discussion - In the design of an IFE reactor, the pressure of the cavity and the pressure exerted on the liquid layer during the time between two heat release pulses are important factors. Figure 6.8.2-12a shows the pressure field in the cavity at different times for the case with lithium as working fluid. The pressure field is shown at the early time of the process. A sudden heat release in the liquid layer causes an intensive evaporation and increase of pressure on the liquid layer. A shock wave is created at this point which moves toward the cavity center. Because of the spherical symmetry of the model, two shocks originated at the same time on opposite walls are reflected at the cavity center. Shock reflection in the cavity center cause an increase in the local pressure. When the reflected shock reaches the wall, another shock

reflection occurs and the wall pressure increases. These multiple shock reflections continue until a steady-state condition is reached and the cavity pressure relaxes to the initial pressure. The transient time for the pressure waves to reach a steady condition is found to be about 50 ms when the working fluid is lithium. The information on the periodic variation of wall pressure is needed in calculations of the pressure loading on the wall, as will be discussed in Section 6.8.2.5.

The same process of shock reflections is also observed for lead as working fluid; the results are shown in Figure 6.8.2-12b. The slight difference of pressure wave behavior in this case is because of different input heats at different times. The transient time in this case is found to be about 150 ms. It is noted that the higher viscosity of lead results in faster damping of the shock waves as compared to the lithium case. The multiple shock reflections on the wall are shown in these figures to cause a periodic variation in the wall pressure.

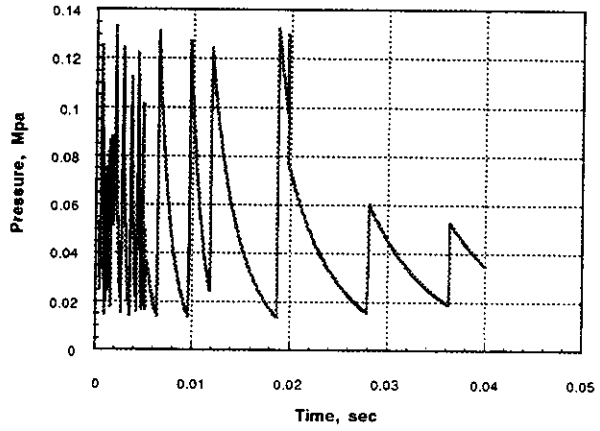

Figure 6.8.2-12a. Instantaneous Uniform Pressure on the Wall with Lithium Vapor

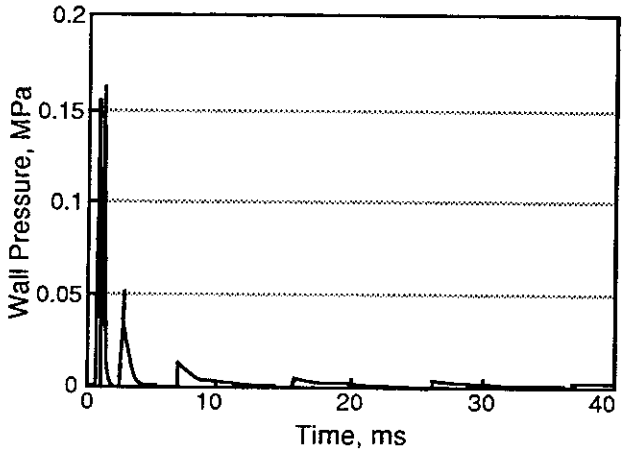

Figure 6.8.2-12b. Instantaneous Uniform Pressure on the Wall with Lead Vapor

References for 6.8.2.4

1. S. V. Patankar, Numerical Heat Transfer and Fluid Mechanics, Hemisphere Publishing Company, New York, 1980.

2. A. K. Runchal, Int. J. Numer. Methods Eng., 24, 1593 (1987).

3. B. Engquist, P. Lotstedt, and B. Sjogreen, Math. Comp., 52, 509 (1989).

4. J. O. Hirschfelder, C. F. Curtiss, and R. B. Bird, Molecular Theory of Gases and Liquids, John Wiley, New York, 1954.

6.8.2.5 Cavity Clearing – Energy released from target microexplosions results in evaporation of substantial mass from the liquid Pb wall protection scheme (of the order of 50-100 kg). This mass must recondense or be evacuated in order to provide a sufficiently low pressure in the cavity gas to allow propagation of the laser or ion beams and the targets. The requirement given for beam and target propagation in Prometheus is 1 mTorr @0°C for the direct-drive target KrF driver and 100 mTorr@0°C for indirect drive target heavy-ion driver. The limit for the laser reactor is determined by electrical breakdown of the cavity vapor and overheating of the unshielded direct drive targets. The channel transport mechanism used for the heavy ion reactor, together with the more robust indirect-drive target, allows a higher cavity base pressure (see Sections 6.5.1.7.4 and 6.5.2.6 on beam and target propagation). The main issue for cavity clearing is whether we can ensure that these low pressures indeed will be obtained.

In addition to the Pb vapor, a small amount (roughly 1 gram) of noncondensible gas remains in the cavity from the plastic case, He reaction product, and unburned D and T. This mass must be evacuated through the vacuum pumping system. The issue of vacuum pumping is treated in Section 6.8.6.

To help understand the nominal cavity gas behavior and transfer of blast energy into the first wall coolant following the explosions, a heat and mass transfer computer model "RECON" was developed. RECON computes the blast energy deposition and solves the time-dependent heat and mass transfer rates in the cavity and film. The initial conditions in the cavity and wall are not known a priori, so RECON solves successive pulses until a quasi-equilibrium condition is obtained. In the following sections, the various parts of the model are described, including mass evaporation and condensation rates, thermal radiation, and conduction into the coolant. (Analysis of energy deposition following a microexplosion is described in Section 6.8.2.2.3.) Results for the base case and parametric studies are then presented for both laser and heavy ion reactors.

Figure 6.8.2-13 shows the geometry of the wall region and the energy transport mechanisms included in the model. The model homogenizes the cavity vapor, assigning a single temperature, pressure, and mass to the cavity volume. The wall region is discretized in the radial direction away from the film surface. All of the energy from the blast ultimately is transferred to the cooling channel.

The crude treatment of the vapor leads to some inaccuracy, particularly in the early part of the pulse; however, the simplicity of the code allows parametric studies to be performed quite easily. For this design concept, the time required for recondensation is limited to a large extent by conduction through the film and into the cooling

channels. Attaining a film surface temperature near the saturation temperature at the required pressure is critical; the RECON model has highly accurate modeling in this region.

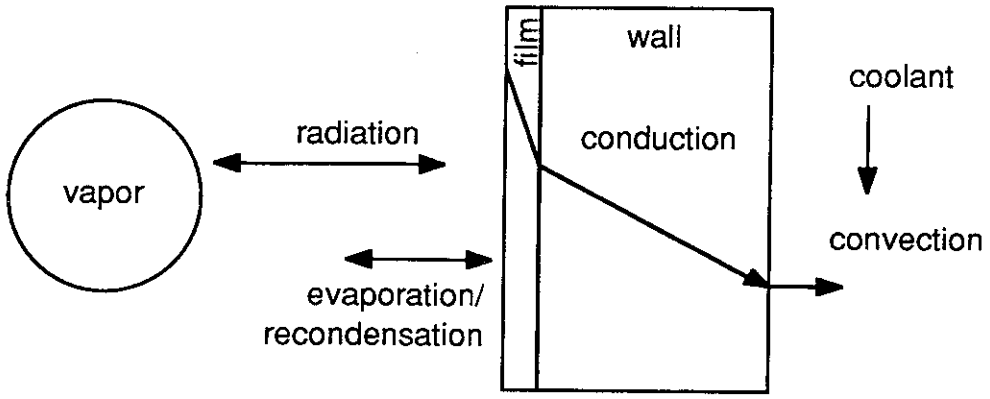

Figure 6.8.2-13 Energy Transport Pathways and Overall Geometry

Mass Evaporation and Recondensation – During the early stages of the cavity response, the cavity vapor is much hotter than the film surface and evaporation occurs. The rate of evaporation, $\dot{m}_e$, is determined from an energy balance between the thermal radiation absorbed at the surface and conduction into the film.

$$h_{fg}\,\dot{m}_e = (q_{rad} - q_k)\,A \qquad (6.8.2\text{-}35)$$

The conduction rate is easily computed from the film temperature gradient at the surface:

$$q_k = k\,\frac{dT}{dx} \text{ at the surface} \qquad (6.8.2\text{-}36)$$

As the cavity vapor cools and q_{rad} drops, recondensation begins. The expression for condensation mass flux used in RECON is based on the work of Pong,[1] which derives a mass diffusion coefficient by the theory of Labuntsov and Kryulov.[2] The mass flux is given by:

$$j = \frac{1.67}{\sqrt{2\pi RT}}\left(P_v - 0.579\,P_{gas}\,\frac{M_{gas}}{M_v}\,P_l\right)\left(1 + 0.515\,\ln\left(\frac{P_v}{P_l}\left(\frac{T_l}{T_v}\right)^{1/2}\right)\right)$$

$$x\left(1 + 4.3\left(\frac{P_{gas}}{P_l}\right)^{0.52}\left(\frac{M_{gas}}{M_v}\right)^{0.74}\left(\frac{T_l}{T_v}\right)^{4.712}\right)^{-1} \qquad (6.8.2\text{-}37)$$

It includes the effect of noncondensible background gas, which in this case would represent He and unburned D and T. Since the molecular weight of these species is so much smaller than that of Pb, a substantial amount of background gas can be tolerated without interfering in the recondensation process. When the heat flux into the surface is greater than the conduction rate, evaporation takes place. Evaporation is assumed to be instantaneous and quantitatively equal to the difference in heat fluxes divided by the latent heat of evaporation.

Thermal Radiation – Thermal radiation in high temperature gases is a complex subject. For this work, we used two simplified models. Radiation heat transfer at lower temperature ranges is based on a classical Stefan-Boltzmann law (T^4 scaling) with an optical thickness parameter (τ) controlled by the user:

$$q_{rad} = \frac{\sigma (T_v^4 - T_l^4)}{1 + \frac{3}{4}\tau} \qquad (6.8.2\text{-}38)$$

The sensitivity of the results to changes in the radiation heat flux was tested by varying τ and observing the effect.

At very high temperatures (above ~100 eV), radiation cooling rates can be obtained from Post.[3]

Prometheus conditions immediately following the blast are at intermediate temperatures of a few eV. In this regime, the vapor is partially ionized. To properly treat the the radiative heat transfer from the gas in this regime, Zel'dovich[4] suggested the following model which is valid for temperatures of a few electron volts and higher.

The cooling rate is expressed as a modified Boltzmann relation:

$$q''' = \frac{4 \sigma T_{vap}^4}{l_1} \qquad (6.8.2\text{-}39)$$

Where T_{vap} is the temperature of the vapor, σ is the Stefan–Boltzmann constant, and l_1 is the frequency averaged photon mean free path. This equation is valid for mean free paths that are less than the characteristic lengths of the cavity. An approximate expression for l_1 is given as:

$$l_1 = \frac{1.1 \times 10^{23} T_{vap}^{7/2}}{N^2 \bar{m} (\bar{m} + 1)^2 \bar{x}_1} \times 10^{-2} \text{ [m]} \qquad (6.8.2\text{-}40)$$

Where N is the gas density in #/cm^3, T_{vap} is the vapor temperature in Kelvin, $\overline{m}$ is the average charge state of the gas, and $\overline{x_1}$ is defined as the ratio of the average ionization potential to the temperature of the vapor:

$$\overline{x_1} = \frac{\bar{I}}{kT_{vap}} \qquad (6.8.2\text{-}41)$$

$\bar{I}$ can be defined in terms of $\overline{m}$ by:

$$\bar{I}\ (\overline{m} + 1/2) = kT \ln\left(\frac{6 \times 10^{21}\ T(eV)^{3/2}}{\overline{m}\ N}\right) \qquad (6.8.2\text{-}42)$$

$\overline{m}$ is obtained from the LIBRA report[5] with an assumption that, at the temperatures of interest, 1 ~ 4 eV (1 eV ~ 11,600 K), the average charge state has a fairly weak dependence on the gas density so it can be assumed that the charge state is independent. LIBRA used $Li_{17}Pb_{83}$ as the liquid metal. Since it is a eutectic, there will be some error incurred from using the charge states presented in LIBRA. However, since lithium lead is 83% lead, the error is believed to be small. The data points for $\overline{m}$ are interpolated between the distinct charge states (i.e., $\overline{m}$ equals 1, 2, 3, etc.) to obtain a continuous function. At these temperatures, the average charge state is approximately constant with the gas density.

The specific energy per unit volume of the lead vapor (ε) can be calculated from:

$$\varepsilon = \frac{3}{2} N (1 + \overline{m}) KT + N Q_{\overline{m}}$$

where Q_m is the summation of the ionization potential from 1 to the charge state m:

$$Q_{\overline{m}} = \sum_{j=1}^{\overline{m}} I_j$$

The discrete function Q_m is turned into a continuous function by interpolating between the discrete values of Q_m. The equation for the specific energy can be inverted to get the temperature of the gas for a given amount of energy being contained in the gas.

Figure 6.8.2-14 gives the internal energy of a gas vs. gas temperature. Note that the continuously changing slope of the curve indicates different levels of ionization. There are no discontinuities shown on the graph as is expected for a single atom; this is because we are dealing with a large number of atoms and these atoms will contain a distribution of energies and different ionization levels.

This model is applied to the transient conditions experienced in a local dry spot, where the high heat flux during the first few fractions of a millisecond cause the sublimation of the SiC first wall structure. This problem is discussed in Section 6.8.5.3.

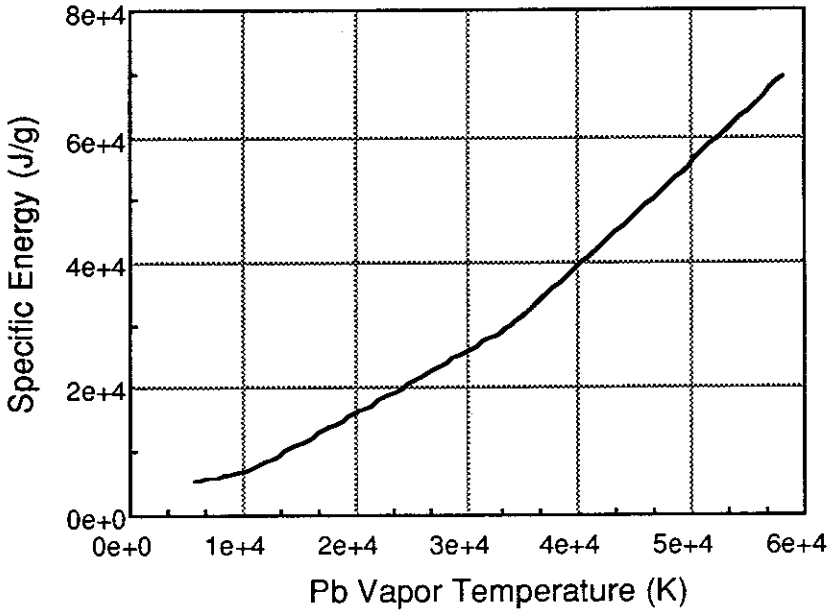

Figure 6.8.2-14 Specific Energy of Pb Vapor vs. Temperature

Conduction in the Film and Wall – The energy equation is finite differenced in the wall:

$$\alpha \frac{\partial^2 T}{\partial x^2} = \frac{\partial T}{\partial t} \qquad (6.8.2\text{-}43)$$

and boundary conditions are applied at the film surface and cooling surface as follows:

$$\frac{k}{\Delta x}(T_1 - T_2) = q_{in} = q_{ec} + q_{rad} \qquad (6.8.2\text{-}44)$$

$$h\,(T_n - T_b) = \frac{k}{\Delta x}(T_{n-1} - T_n) \qquad (6.8.2\text{-}45)$$

Transient conduction at the film surface is an important heat transfer mechanism. The grid is tailored with many grid points near the surface and a stability condition is imposed on the overall time step:

$$\Delta T < 0.5 \frac{(\Delta x)^2}{\alpha} \qquad (6.8.2\text{-}46)$$

Results – This section is divided into two main parts: (1) presentation of base case clearing results for the laser and heavy ion reactors, and (2) parametric studies. First, a few simple observations are given to provide a better understanding of recondensation in the cavity. The behavior following a microexplosion can be divided into roughly four phases.

(1) At or near t=0, x-ray energy is deposited in the cavity gas and in the first few microns of the protective film. Only ~5 kg of Pb is evaporated and the cavity gas temperature reaches several eV.
(2) In the first millisecond, thermal radiation from the cavity gas is very intense and causes "secondary evaporation" from the surface. The mass of Pb in the cavity grows to ~100 kg. Thermal radiation is so rapid that the cavity gas pressure decreases even though the mass increases. Figures 6.8.2-15 and 16 show example cavity pressure and mass histories following the blast.
(3) After conduction near the surface exceeds the rate of thermal radiation, the recondensation phase begins. At early times, conduction is very efficient because the temperature gradient near the surface is high as a result of the energy deposition from the blast. Recondensation is driven by the pressure difference between the cavity gas and the saturation pressure at the surface, so the rate steadily decreases.
(4) No clear boundary exists between the third and fourth stages. However, as the cavity pressure approaches the saturation pressure at the surface, the condensation rate can slow significantly. In this stage, the ultimate cavity pressure is determined primarily by conduction through the bulk of the film and wall and by the bulk coolant temperature.

In the wetted wall cavity, the recondensation process is limited by heat conduction through the wall and into the first wall cooling system. In order to obtain the best performance, the structures between the chamber and the first cooling channel must have high thermal conductivity and be kept as thin as possible. It is important not to overload the system with too high a power density. A simple heat removal formula was included in the Prometheus system codes:

$$\frac{\dot{Q}_w}{A} < \frac{k_{eff}\,(T_{sat} - T_c)}{\delta} \qquad (6.8.2\text{-}47)$$

This formula was then tested against several RECON runs and correction factors applied to make it consistent with the more detailed simulations.

The saturation pressure vs. temperature is given by:

$$T_{sat}(Pb) \sim \frac{11290}{11.34 - \log_{10}(p)} \qquad (6.8.2\text{-}48)$$

This is plotted in Figure 6.8.2-17. Since cavity pressure limits are traditionally expressed at 0°C, the curve is also shown in temperature-corrected form. Note, operation at 1 mTorr requires that the surface temperature be cooled below ~950 K; operation at 100 mTorr requires a surface temperature below ~1150 K.

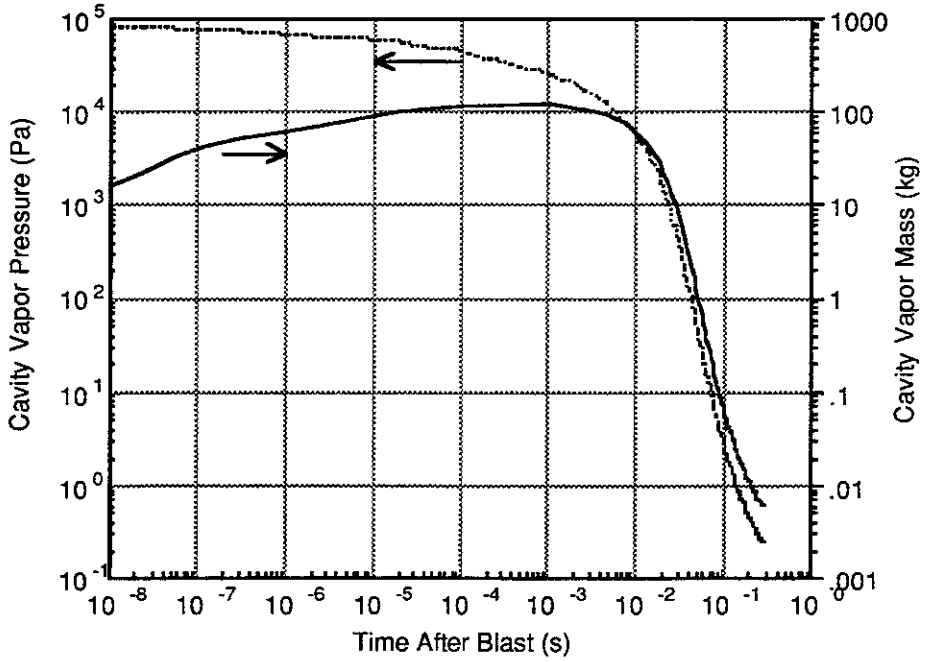

Figure 6.8.2-15 Cavity Vapor Pressure and Mass Histories for Prometheus-L

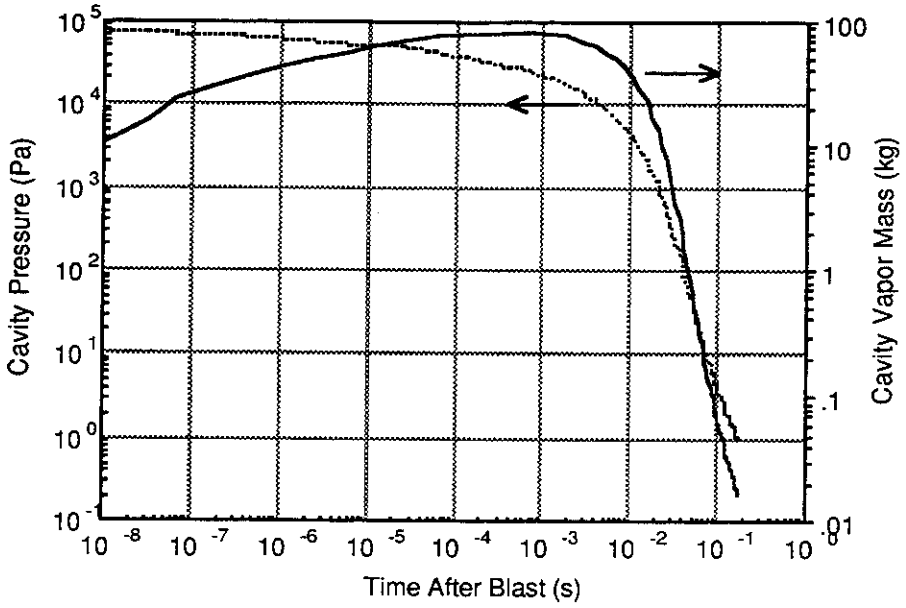

Figure 6.8.2-16 Cavity Vapor Pressure and Mass Histories for Prometheus-H

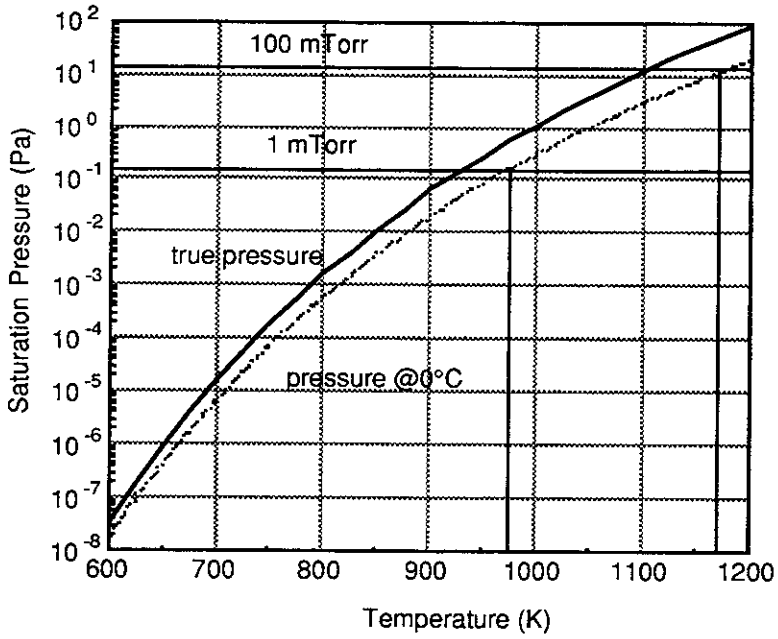

Figure 6.8.2-17. Saturation Pressure of Pb (Solid Line) and Saturation Pressure Corrected to 0°C (Dotted Line)

Base Case Results – Results are shown below for Prometheus-L and -H. Figures 6.8.2-18 and 19 show the cavity vapor temperature and pressure histories as calculated by RECON using the input parameters shown in Table 6.8.2-9. Based on

this analysis, the laser cavity pressure drops below 1 mTorr (@0°C) before the next shot (at 0.25 s) if the cavity cylindrical section height is 10 m. With a height of 5 m, the base pressure is ~3 mTorr, which is judged to be acceptable (the uncertainties in the pressure limit as well as the recondensation calculation are high enough that strict adherence to the 1 mTorr limit is not considered mandatory). The final pressure for the HI case is ~10 mTorr (@0°C).

Table 6.8.2-9 Base Case Parameters

	Laser	HI	Units
Bulk Coolant Temperature	648	648	K
Pb Film Thickness	0.5	0.5	mm
SiC Wall Thickness	5	5	mm
Cavity Radius	5.0	4.5	m
Cavity Cylinder Height	5.0	4.5	m
Surface Area	471	382	m^2
Volume	916	668	m^3
X-ray Yield	31	46	MJ
Debris Yield	107	159	MJ
Rep Rate	5.6	3.5	Hz
Emissivity	1	1	
Noncondensible Gas Pressure	3	100	mTorr @ 800 K

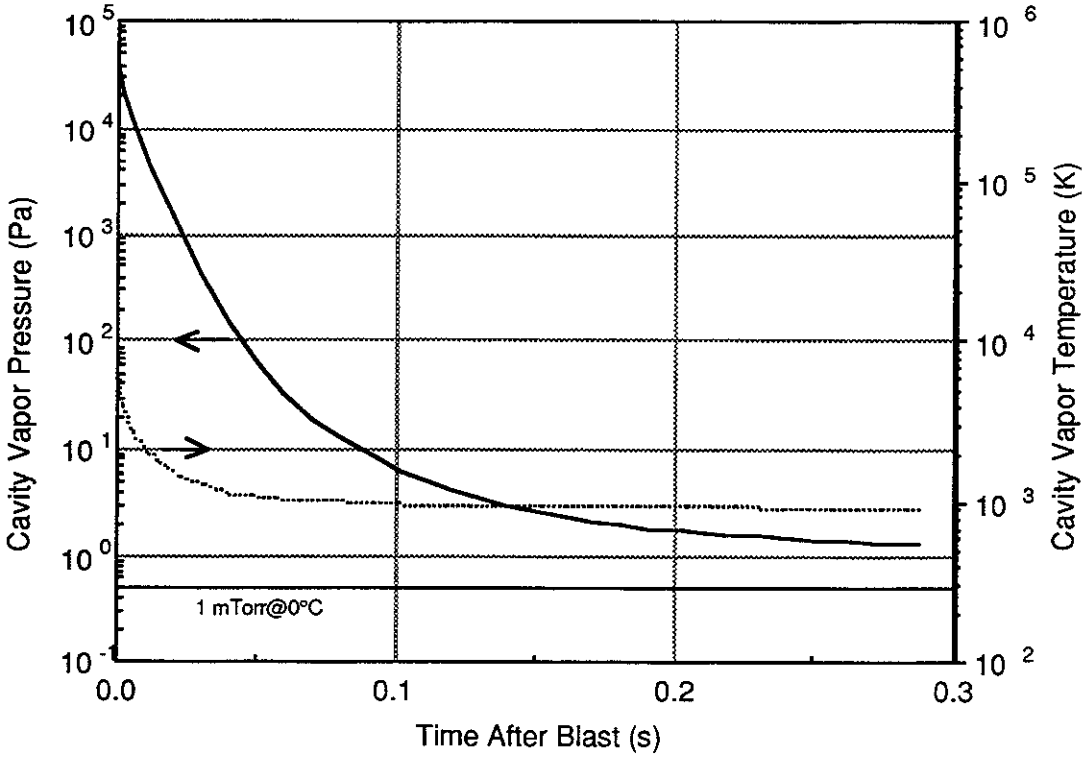

Figure 6.8.2-18 Base Case Cavity Vapor Temperature and Pressure Histories for Prometheus-L

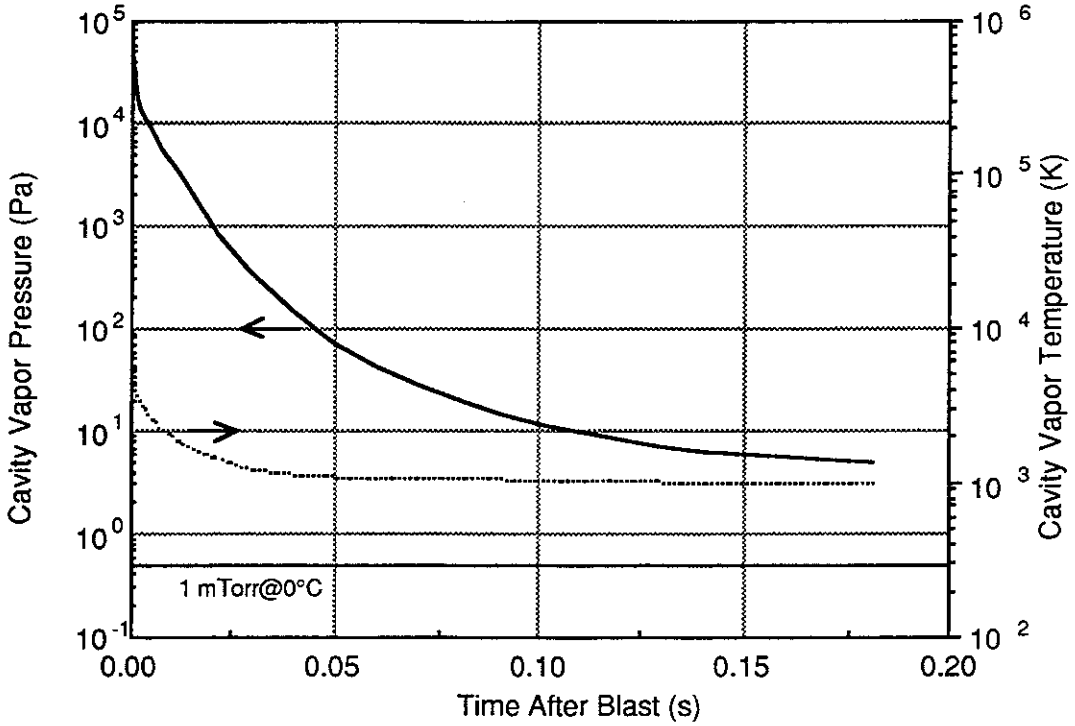

Figure 6.8.2-19 Base Case Cavity Vapor Temperature and Pressure Histories for Prometheus-H

Most of the initial blast energy is absorbed in the cavity gas. Approximately 5 kg of Pb are evaporated by direct energy deposition. The initial (averaged) cavity vapor pressure and temperature are estimated as 49 kPa and 550,000 K respectively. A much larger amount of Pb is evaporated due to rapid radiation cooling of the cavity vapor. Before the recondensation phase begins, about 80 kg of Pb (10 μm) are evaporated.

Figure 6.8.2-20 shows the temperature at the surface of the film and at the interface between the film and SiC structure. The SiC temperature is always well below the compatibility limit with Pb (~1000°C). The surface temperature drops very quickly immediately following the blast and asymptotically falls towards the bulk coolant temperature. The ultimate cavity vapor pressure is very sensitive to this slow conduction-dominated phase of the process because the vapor pressure is strongly temperature-dependent. By maintaining a thin first wall and low coolant temperature, adequate recondensation can always be assured (within the scope of this simplified model).

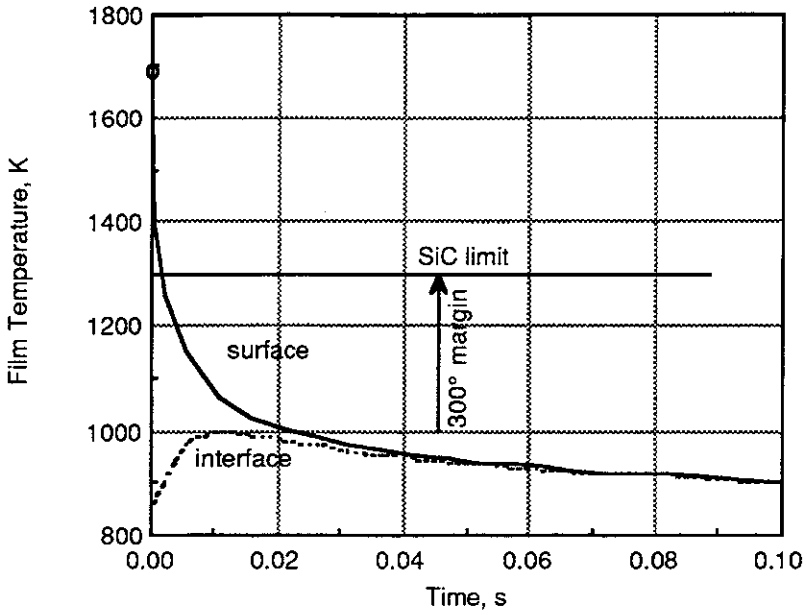

Figure 6.8.2-20. Base Case Temperatures at the Film Surface and Interface Between the Film and SiC Wall for Prometheus-L

Parametric Studies – To aid in the design of the cavity and to provide a better understanding of the behavior following the blast, a series of parametric studies were performed using RECON. A base case was defined using the laser reactor parameters listed in Table 6.8.2-9 except that, for these cases, the background (non-condensible) gas pressure was 1 mTorr.. Variations were made in the repetition rate, background pressure of non-condensible gases, and the cavity geometric parameters (radius, area and volume).

(1) Effect of Repetition Rate Under Constant Power - For this study, the total surface power was held fixed at 718 MW. The repetition rate was varied from 3 to 8 Hz while adjusting the yield to maintain constant power. Figure 6.8.2-21 shows the resulting cavity pressure at the end of a pulse. As the repetition rate increases, the cavity base pressure also increases, even though the yield is decreasing proportionately.

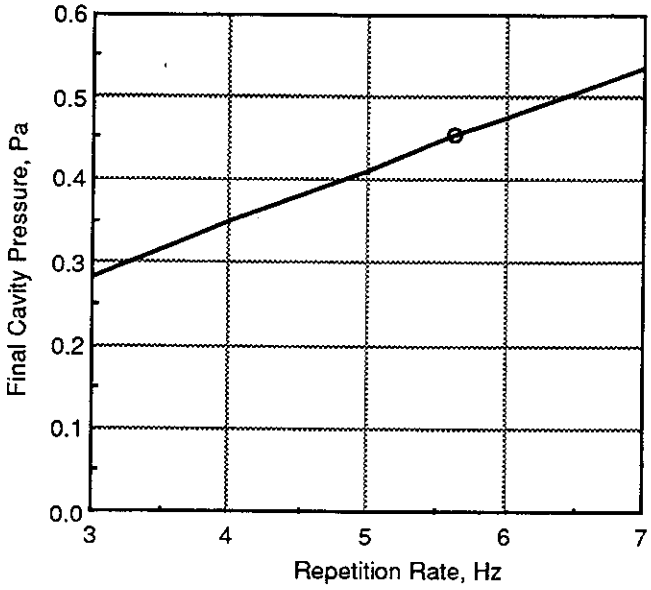

Figure 6.8.2-21 Effect of Rep. Rate on the Cavity Pressure Following a Blast

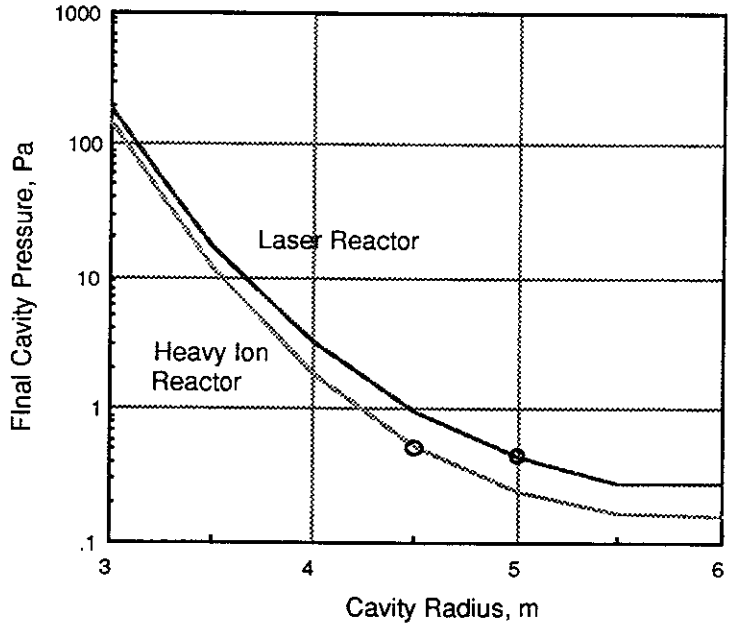

Figure 6.8.2-22. Effect of Increasing the Cavity Size on the Cavity Pressure Following a Blast

(2) Effect of Geometric Parameters - Figure 6.8.2-22 shows the effect of varying the radius for both the laser and heavy ion reactor cavities. The area and volume were also changed to maintain constant aspect ratios. The values used were:

Radius (m)	Area (m^2)	Volume (m^3)
3	170	198
3.5	231	314
4	302	469
4.5	382	668
5	471	916
5.5	570	1220
6	679	1583

Above ~5 m radius, little additional reduction in pressure is made. Below ~4 m, the pressure rises rapidly.

Parametric studies were also performed by varying the surface area and volume independently. Of course, in a real system, the dimensions would all change in a self-consistent manner. For the purpose of this study, we varied only one at a time in order to determine the true effect of each separate parameter. Figures 6.8.2-23 and 24 show the results. The effect of changing the wall surface area is very pronounced below ~400 m^2. It is impossible to achieve pressures below ~0.05 Pa which corresponds to the vapor pressure at the coolant outlet temperature.

Figure 6.8.2-24 shows the effect of changing the cavity volume with the surface area held constant. The pressure decreases as the volume decreases, subject to the same limitation as above (due to the vapor pressure at the coolant outlet temperature). This trend seems counter-intuitive; one might expect the clearing time to improve with larger chambers. It is important to recall that the surface area effect is not present here, as the area is fixed.

Figure 6.8.2-25 shows the pressure history for two cases with different volumes. The volume could be increased without changing the area by making the cavity more spherical. The curves show an interesting result. Initially, a larger cavity has a lower pressure, because both cases have roughly the same mass evaporated (evaporated mass depends primarily on the yield). However, the time to recondense is longer for larger volumes. This is because the recondensation mass flux is driven by the pressure in the cavity. At a given pressure, the mass flux will be the same in both cases, but the amount of mass to be removed is greater with the greater volume.

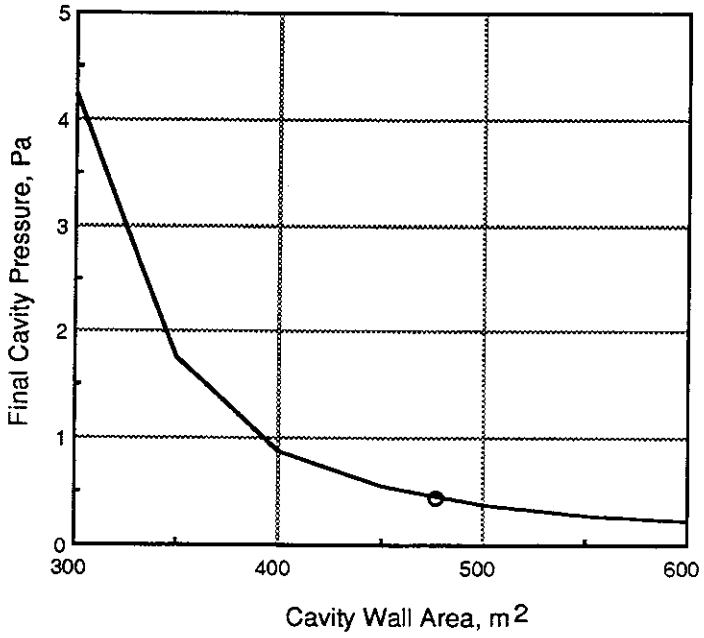

Figure 6.8.2-23 Effect of Changing the Cavity Area with the Volume Fixed

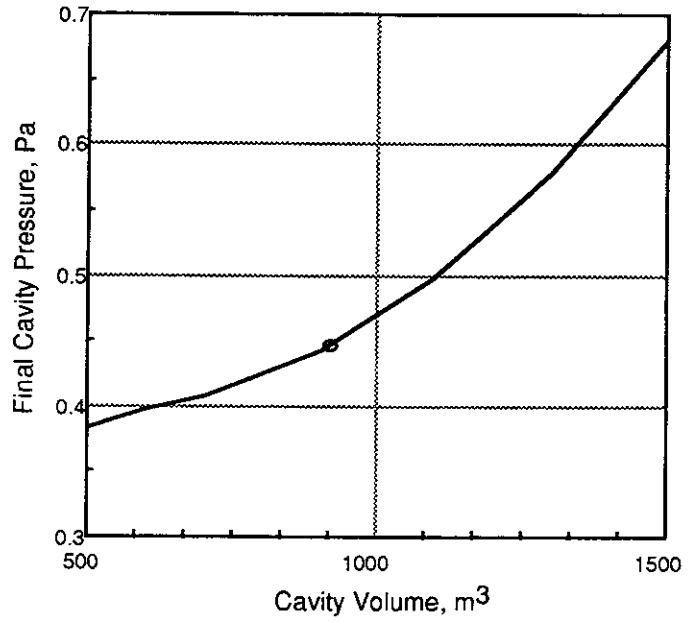

Figure 6.8.2-24 Effect of Changing the Cavity Volume with the Area Fixed

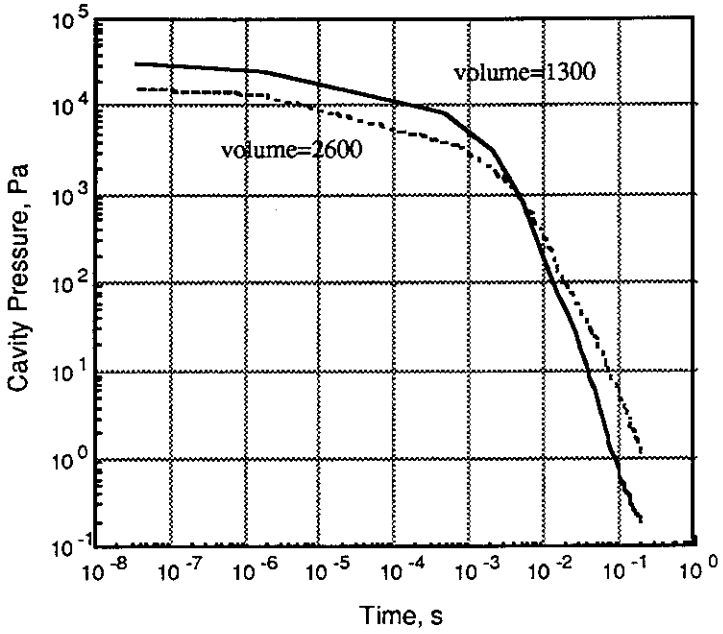

Figure 6.8.2-25 Effect of Increasing the Cavity Volume on the Pressure History

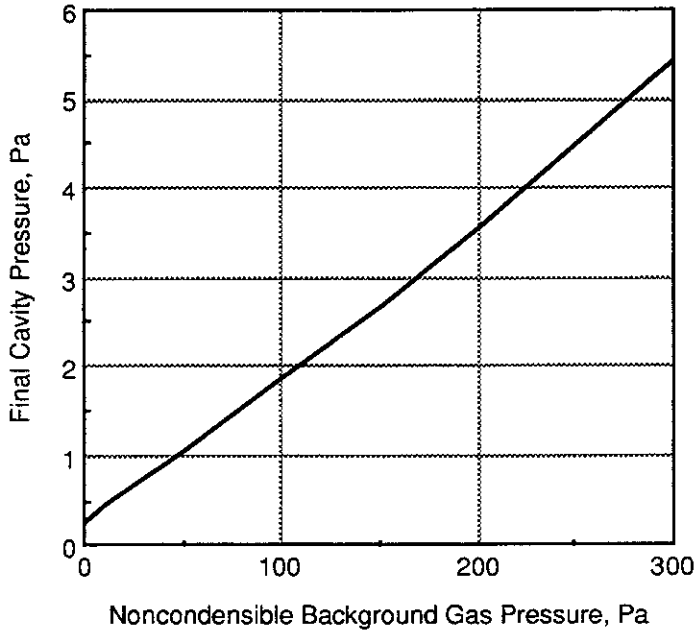

Figure 6.8.2-26 Effect of Non-condensible Gas Pressure on the Final Cavity Pressure

The results show that larger volume results in higher pressure at the end of the pulse (or longer time to recondense to a given pressure). A larger cavity volume results in lower initial pressure, because the initial mass of Pb evaporated depends primarily on the total yield. However, the rate at which mass is evacuated is smaller for larger volumes. Recondensation is driven by the pressure in the cavity. At a given pressure, the mass flux will be the same in both cases, but the amount of mass to be removed is greater with the greater volume.

(3) Effect of Non-condensible Gas - The pressure of non-condensible gas was increased to determine how much vacuum pumping is needed. For this calculation, the average Z was set to 2. Figure 6.8.2-26 shows the results.

References for 6.8.2.5

1. L. Pong, et al.,"Liquid Metal Condensation in the Cavity of the HIBALL Heavy Ion Fusion Reactor," Nuc. Eng. and Design/Fusion 3, 47-57 (1985).

2. D. A. Labuntsov and A. P. Kryukov, "Analysis of Intensive Evaporation and Condensation," Int. J. Heat Mass Transfer, Vol. 22, 989 (1979).

3. E. Post, et al., "Steady State Radiative Cooling Rate for Low Density High Temperature Plasmas," Atomic and Nuclear Data Tables (20), p 397, 1977.

4. Ya. B. Zel'dovich and Yu. P. Raizer, "Physics of Shock Waves and High-Temperature Phenomena," Academic Press, New York and London, 1966.

5. B. Badger, et al., "LIBRA – A Light Ion Beam Fusion Conceptual Reactor Design," Univ. of Wisconsin, UWFDM-800, July 1989.

6.8.2.6 Film Flow

Introduction – In this section, the major characteristics of the first wall protective film are described and several special problem areas are analyzed.

There are several possible methods to inject the wall protectant and control its thickness. In the Prometheus baseline design, the liquid lead film is supplied partly by seepage through the porous first wall coolant channels and partly from an injector at the top of the upper hemisphere (see Figure 6.8.2-1). The seepage flow rate must be sufficient to maintain good coverage, but not so high as to detach or destabilize the film. As Pb reaches the surface of the first wall, it forms a continuous film which flows to the bottom of the cavity by gravity. This drainage is desired to maintain a clean surface. The film flow removes condensible impurities generated from target debris and, to some extent, by wastage of the first wall panels.

Additional Pb is injected into the upper hemisphere to ensure coverage of the upper end cap without dripping into the cavity. The inertia of the jet is adequate to provide attachment onto the entire surface. This jet is allowed to flow down the vertical section of the first wall and ultimately into the drain. Protection of inverted surfaces is a special problem for this type of wetted wall chamber and several solutions have been proposed and analyzed.

Design of the film system was undertaken with several key objectives in mind. The thickness of the film is a key parameter, since Prometheus uses primarily conduction through the film to remove the surface heating power. Calculations are described here for the evolution of the film thickness and velocity, subject to several constraints imposed on the flow. For example, a minimum film thickness is required to ensure adequate protection against the blast but, if the film becomes too thick, it loses its ability to conduct the surface heating power to the cooling channels. A minimum jet velocity is required to ensure attachment onto the upper hemisphere; however, higher velocities entail thicker films. The calculations described below were performed in order to define the allowable range of operating conditions and to optimize the film flow system.

There are several design options which were also considered:

(1) If the film thickness is too large, then conduction alone may be insufficient to remove the surface heating power. The possibility for convective heat removal was explored.
(2) Protection of the upper end cap presents unique problems. The requirements for jet injection at the upper end cap provide a less attractive film on the remainder of the cavity wall if this jet is allowed to fall to the bottom of the cavity.

Extraction of this jet at the upper hemisphere and optimization of the film thickness along the vertical section was considered.

(3) Finally, control of the film thickness could be made considerably easier with the use of guiding magnetic fields. Modest field strengths could maintain a much thinner film than that available from an inertial jet. Enhanced stability of the film would be an additional benefit.

Flow Characteristics – In order to maintain the film on the upper hemisphere, a jet is injected at the top. The relatively high speed required to keep the jet attached to the wall leads to turbulence in the film. A number of previous studies have explored the wave structure of a vertical turbulent falling film.[1,2] These studies indicate that the wave structure is complex—there appear to be several classes of waves and each class has certain random features. Waves formed at the film interface appear to be a combination of large waves with small ripples superimposed on the large waves. Film waviness is complicated further by variations in both film thickness with film travel. An illustration of turbulent film wave structure given in Chu and Dukler 's study is shown in Figure 6.8.2-27 which indicates that various film thicknesses can be observed in this

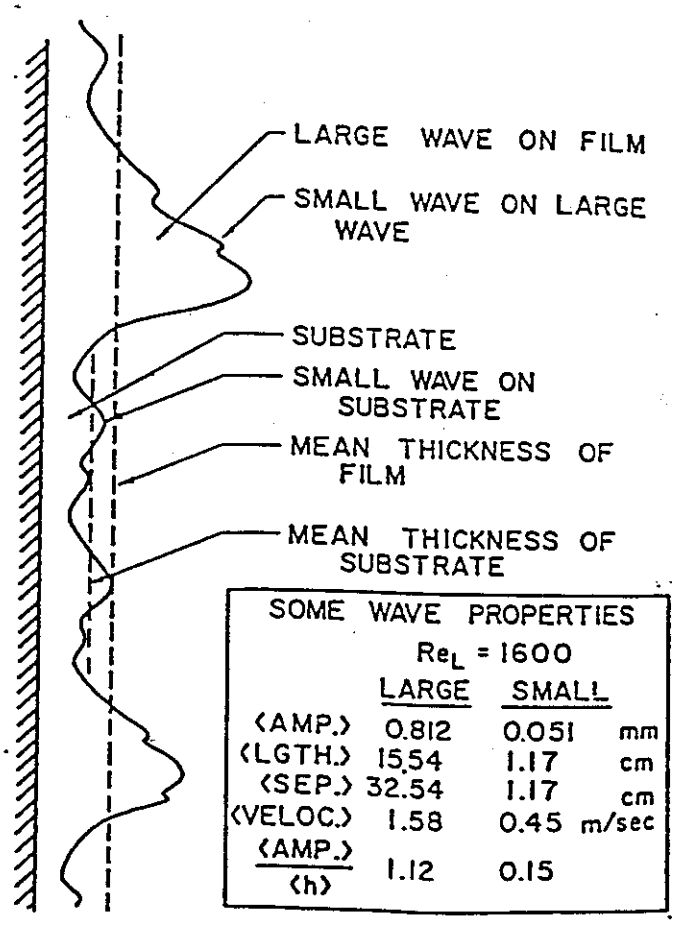

Figure 6.8.2-27. Identification of Wave Classes[1]

type of film. While using this turbulent liquid film for the first wall protection, the concern is whether a minimum film thickness can be greater than the required film thickness for x-ray and debris protection (such as 100 mm). The experimental study of Takahama[2] shows that the minimum film thickness decreases toward the entrance region, however, almost constantly independent of Reynolds number and the longitudinal distance. The minimum film thickness identified in their study was about 300 mm. Figure 6.8.2-28 illustrates their results of film thickness variations along the longitudinal direction.

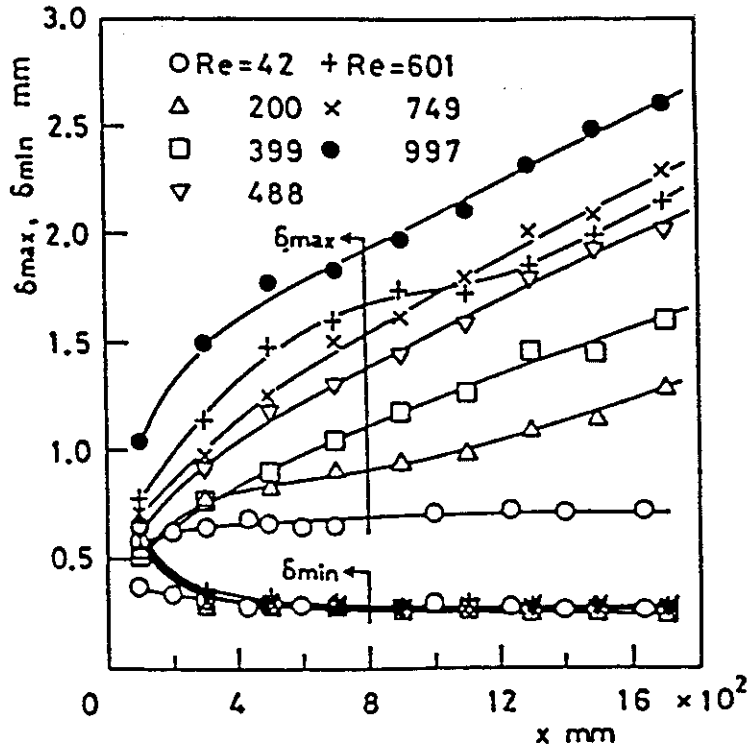

Figure 6.8.2-28. Longitudinal Distribution of Maximum and Minimum Film Thickness[2]

Flow through the Porous Wall – The porous first wall structure allows coolant to seep from the cooling channels onto the wall surface. The supply rate must be high enough to provide good coverage, but not so high as to impart momentum into the film and cause detachment. Ideally, the permeability would be tailored to provide optimum flow control but, in this work, we assume a constant permeability.

The seepage rate depends on the cooling channel pressure and the permeability of the wall, and is estimated using Darcy's formulation:[3]

$$-\nabla P - \frac{\mu}{\kappa} v \delta_{wall} = 0 \qquad (6.8.2\text{-}49)$$

where v is the average seepage velocity, P is the pressure, μ is the dynamic viscosity of the fluid, and κ is the permeability of the wall. The permeability is calculated as:

$$\kappa = \frac{d^2}{175}\frac{\varepsilon^3}{(1-\varepsilon)^2} \qquad (6.8.2\text{-}50)$$

where d is the fiber diameter, ε is the porosity, and the seepage rate q^* is defined by:

$$q^* = v\,A_l \qquad (6.8.2\text{-}51)$$

where A_l is the lateral flow area.

Figure 6.8.2-29 shows the baseline pressure distribution along the coolant channel and the resulting seepage rate.

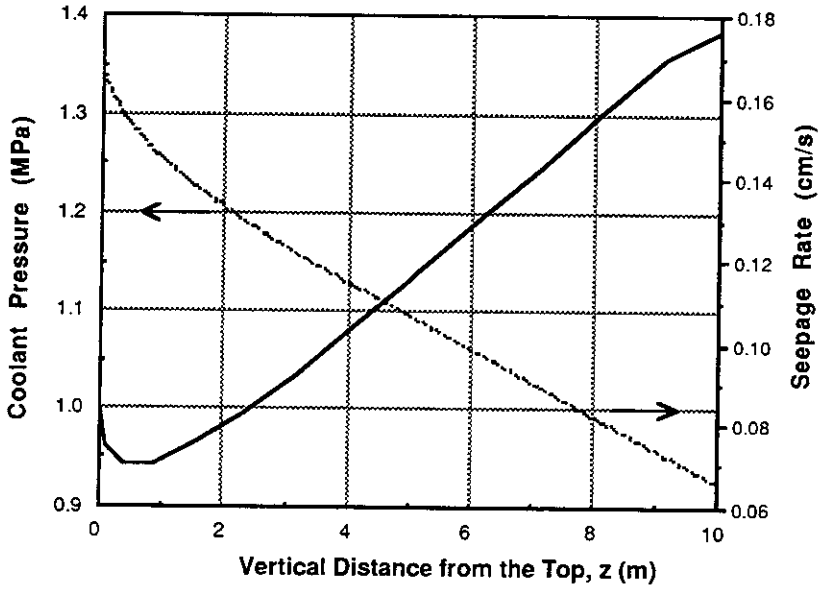

Figure 6.8.2-29. Baseline Pressure Distribution and Seepage Rate Along the First Wall

Basic Film Flow Equations – The film flow is driven mainly by gravity, which is then balanced by the drag along the wall and the flow accelerational force. The force balances in the normal and tangential directions for a fluid element are shown schematically in Figure 6.8.2-30 and are written as:

$$\rho\frac{u^2}{r_v}\delta = \frac{2\sigma\cos(\theta)}{R} + \frac{2\sigma}{r_v} + \rho g_c \delta \sin(\theta) \qquad (6.8.2\text{-}52)$$

$$\rho u \delta \frac{\partial u}{\partial l} = \rho\, g_c\, \delta \cos(\theta) - \tau_D \qquad (6.8.2\text{-}53)$$

where ρ is the fluid density, u is the liquid film velocity in the tangential (flow) direction, δ is the film thickness, r_v is the radius of curvature, σ is the surface tension, g_c is the

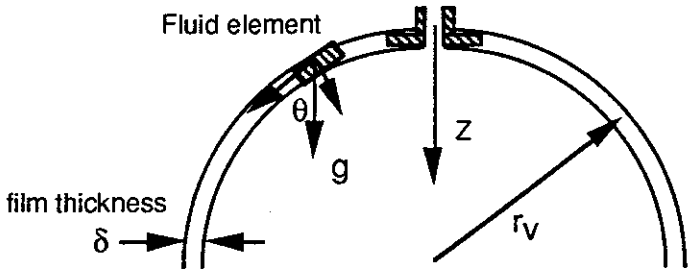

Figure 6.8.2-30. Illustration of Force Elements Acting on the Upper Wall Film

acceleration due to gravity, τ_D is the wall friction force exerted on the fluid along the flow direction, θ is the angle that the tangent to the fluid element forms with the z axis, and l is the distance measured along the flow direction.

The mass conservation equation is also needed:

$$\frac{\partial(uA)}{\partial l} = q^* \qquad (6.8.2\text{-}54)$$

where A is the film cross-sectional flow area, u is the mean velocity of flow in the longitudinal direction, and q^* is the seepage inflow rate per unit length.

To solve these equations, an expression is needed for the wall friction force in Eq. 6.8.2-53. In general, the turbulent wall friction force is expressed in terms of the friction factor as:

$$\tau_D = \frac{f}{4\delta}\frac{u^2}{2g_c} \qquad (6.8.2\text{-}55)$$

where f is the friction factor.

There are several possible methods to evaluate the friction factor for turbulent film flow. For Reynolds numbers less than 100,000, the frictional factor given by the Blasius formula[4] provides the closest estimate of the turbulent film thickness when compared to the empirical correlation of turbulent falling film thickness (δ_t) presented by Gimbutis.[5] The Blasius formula for friction factor is given by:

$$f = \frac{0.316}{Re^{0.25}} \qquad (6.8.2\text{-}56)$$

where the Reynolds number is defined as:

$$Re = \frac{4\psi}{\rho\nu_f} \qquad (6.8.2\text{-}57)$$

and ψ is the flow rate:

$$\psi = u\,\delta_t\,\rho \qquad (6.8.2\text{-}58)$$

The Gimbutis's turbulent film thickness (δ_t) is expressed as:

$$\delta_t = 0.136\left(\frac{\nu_f}{g}\right)^{1/3} Re^{0.583} \qquad (6.8.2\text{-}59)$$

Before solving for film velocities and thicknesses, two important constraints must be considered: (1) the minimum required thickness to ensure protection of the substrate, and (2) the minimum velocity required to maintain attachment on the upper end cap.

Minimum Film Thickness – The minimum required film thickness is determined from the evaporation caused by target explosions. This depends on the target energy spectrum, yields, absorption characteristics of the film material, and vapor radiation processes. Energy deposition is covered in detail in Section 6.8.2.3. The depth of evaporation was estimated there to be only about 10 μm per shot. This amount of Pb will be condensed back into the film before the next shot. While under ideal conditions only ~10 μm is required, additional thickness is allowed for nonuniformities and extra margin. For this study, we assume a minimum film thickness of 100 μm.

Requirement for Attachment on the Upper End Cap – The film velocity in the upper end cap must be sufficiently high such that the film remains attached to the surface. Since the film velocity and thickness are related (by Eq. 6.8.2-59), higher velocities entail thicker films. To minimize the film thickness, it is desirable to operate near the attachment limit.

The solution of Eq. 6.8.2-52 provides the minimum velocity required to prevent the fluid from separating from the wall. At different locations on the curved surface, there is a different minimum velocity. Figure 6.8.2-31 shows these minimum required velocities as a function of distance away from the upper end cap (radius = 5 m). The minimum velocity decreases as the flow proceeds downstream; the highest minimum velocity is 7 m/sec. With this minimum velocity and the minimum film thickness for x-ray and debris absorption (~100 μm), the fluid is always turbulent, with Reynolds number larger than the critical film Reynolds number (Re_c~1600).

For each location on the upper end cap, the turbulent film thickness (based on Gimbutis's formula) and the mass flow rate are estimated using the minimum velocities from Figure 6.8.2-31. The results are shown in Figure 6.8.2-32. They indicate that, in order to maintain the flow attached to the surface, the film thickness must be greater than 6.4 mm. The minimum volumetric flow rate increases first, reaches a peak value, and decreases as the flow proceeds to downstream locations.

Once the film travels to the straight portion of the cavity wall, there is no minimum film velocity required. In fact, after the peak required flow rate is achieved (just beyond 1 m from the top), a thinner film can be maintained and control of the film becomes easier.

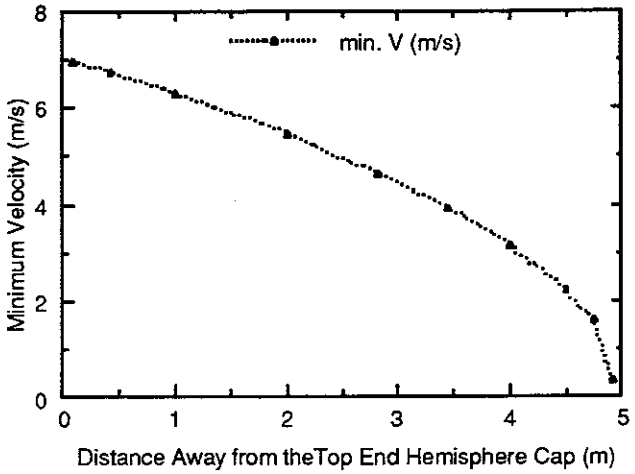

Figure 6.8.2-31. Minimum Required Film Velocity for Attachment on the Upper Hemisphere Wall

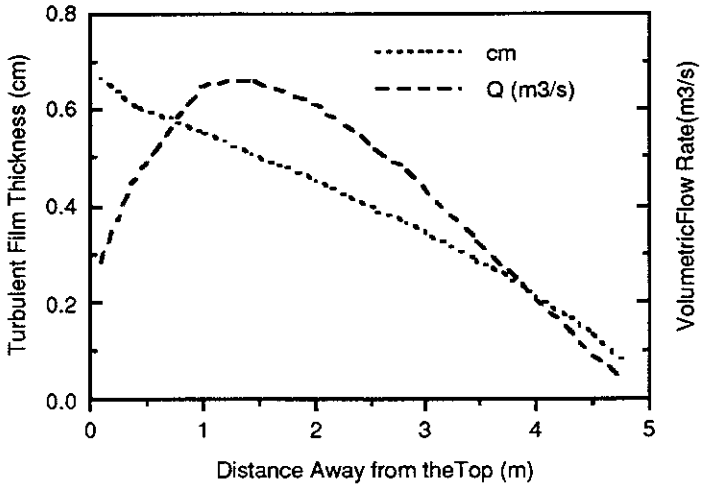

Figure 6.8.2-32. Turbulent Film Thickness and Minimum Volumetric Flow Rate for Attachment

One of the major design options for film control is to remove the jet at this point and use an injection scheme primarily supplied by seepage from the coolant channels.

Results – Eqs. 6.8.2-53 and 6.8.2-54 were solved for the film thickness and velocity along the flow direction for different initial flow rates and wall characteristics. Example results are shown in Figure 6.8.2-33 for film thickness and Figure 6.8.2-34 for velocity.

There are several parameters which affect the film characteristics. These are injection angle, film injection velocity and initial film thickness, wall permeability, and lateral supply rate. Two cases were analyzed: Case 1 has a relatively modest injection velocity of 15 m/s and Case 2 increases this to 40 m/s. For both cases, the film flow is initiated by injection at an angle of 82° (defined as the angle between the flow and the direction of gravity) with a wall permeability of 1.764×10^{-14} m^2. Table 6.8.2-10 summarizes the parameters.

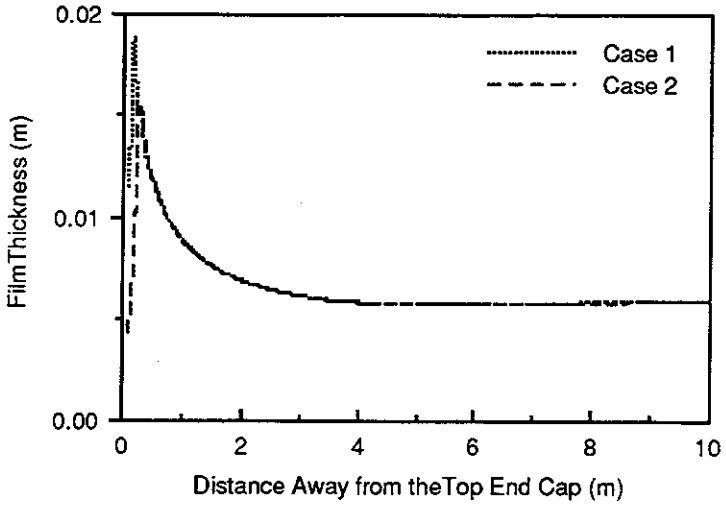

Figure 6.8.2-33. Film Thickness as a Function of Distance Away from the Top End Cap

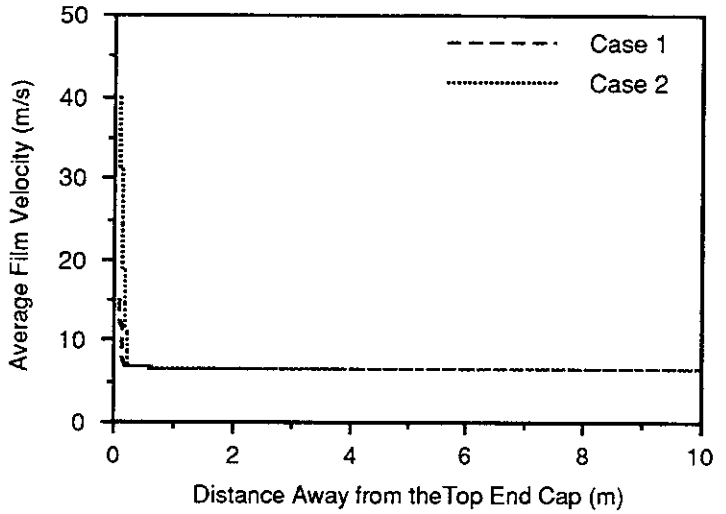

Figure 6.8.2-34. Average Film Velocity as a Function of Distance from the Top End Cap

Table 6.8.2-10 Summary of Cases Analyzed

Parameter	Case 1	Case 2
Injection Velocity	15 m/s	40 m/s
Initial Thickness	1.15 cm	0.43 cm
Maximum Thickness	1.9 cm	1.6 cm
Ultimate Thickness	0.6 cm	0.6 cm

Beyond the injector region, there is little difference between the two cases. In each case, the velocity decreases immediately due to the wall drag. The film thickness increases first due to the reduction of film velocity and later decreases because of the expansion of the flow area. The maximum film thickness decreases from 1.9 to 1.6 cm as the injection velocity increases from 15 to 40 m/s. For both cases, the ultimate film thicknesses are about 0.6 cm.

These film thicknesses are much larger than that required for x-ray and debris absorption and may be too large for removing heat by conduction. To reduce the film thickness on the curved hemispheric wall, the lateral supply from the main stream can be reduced by decreasing the wall permeability once the flow reaches the peak point.

Convective Heat Transfer in the Film – The analysis of film flow on the upper hemisphere indicates that maintaining a film smaller than a few mm is not possible. As the film thickness grows, heat removal by conduction is reduced. In order to prevent high surface temperatures (which prevent high repetition rates), good convection heat transfer may be required.

Thermal analyses were performed for two different cases. In both cases, the film is supplied by both injection at the top and laterally from the cooling channels. Parameters were chosen in order to provide as uniform a film thickness as possible. In Case 1, the flow injection rate at the top end cap is maximized and the porosity of the wall is 15%. In Case 2, the lateral supply rate is maximized and the porosity of the first wall is 30%.

The total amounts of flow from the lateral supply for Cases 1 and 2 are 4% and 35% of the ultimate flow rate, respectively. Under these conditions, the lateral momentum flux is only a few percent of the longitudinal momentum flux, so that 1-D analysis should be adequate.

Results are shown in Figures 6.8.2-35 and 36. The film flow is initiated by injecting the flow at an angle of 82° (about 10 cm away from the top). Initial velocities of 35 and 40 m/s and initial film thicknesses of 4 and 2.5 cm are assumed for Cases 1 and 2, respectively. The results show that in each case the velocity decreases very rapidly initially due to wall drag. The film thickness first increases due to the reduction of the film velocity, and then decreases later because of the increase in flow area.

For Case 1, the peak film thickness is 5.4 cm and the ultimate thickness is 1.54 cm. For Case 2, the peak, mean film thickness is about 3.9 cm and the ultimate, mean film thickness is about 1.6 cm. If the initial velocity can be further increased, a more uniform mean film thickness can be obtained.

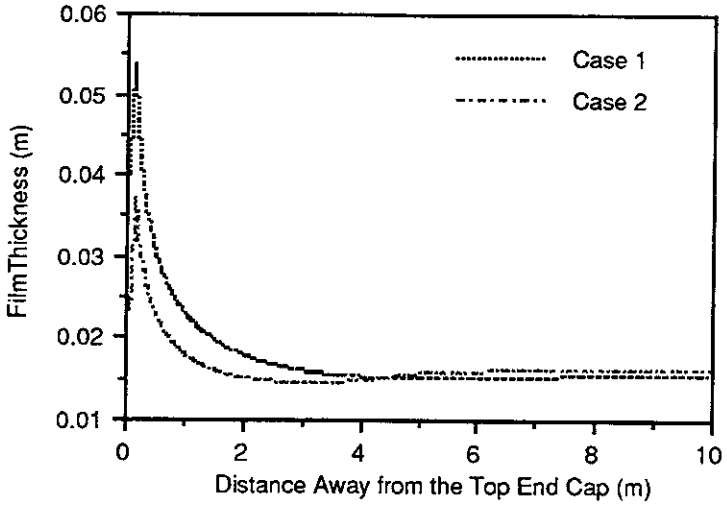

Figure 6.8.2-35. Film Thicknesses as a Function of Distance Away from the Top End Cap

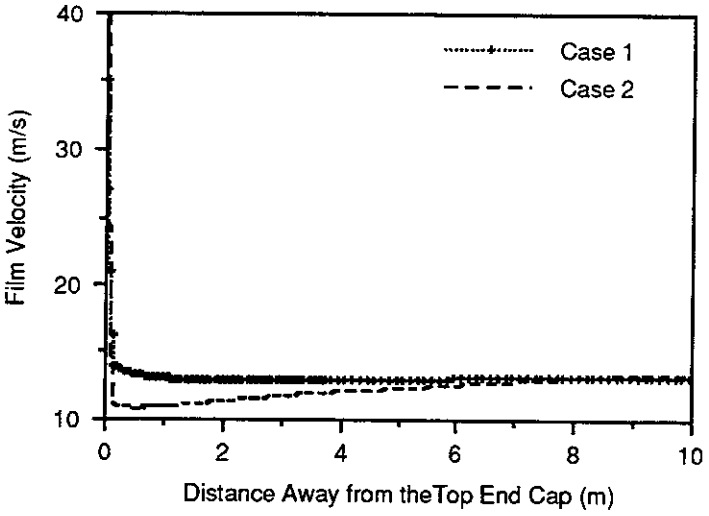

Figure 6.8.2-36. Film Velocities as a Function of Distance Away from the Top End Cap

The concerns of using a couple of cm thick film are whether the temperature on the first wall is beyond the design limit and whether the temperature on the film surface is too high for the condensation to take place. At pressure of $1x10^{-3}$ torr, the saturation temperature is about 627°C; the saturation temperature increases to 838°C as the pressure increases to $1x10^{-2}$ torr. In order to have a significant amount of condensation on the film surface, the film surface temperature should be less than 627°C for laser driven IFE and 838°C for heavy ion driven IFE. The film heat transfer coefficient given by Lee[6] is examined for this purpose. The turbulent film heat transfer coefficient for liquid metal is of the same order as the laminar heat transfer coefficient. The non-dimensional laminar heat transfer coefficient for condensation was expressed in terms of Reynolds number and written as:

$$\left(\frac{\nu^2}{g_c}\right)^{1/3}\frac{h_{av}}{k} = 1.47\,Re^{-1/3} \qquad (6.8.2\text{-}60)$$

At Reynolds number of 8.5×10^5, which corresponds to the Reynolds number at the vertical section of the reactor chamber, the heat transfer coefficient is estimated as 1.51×10^4. For heat flux of 2.7×10^6 W/m^2, the film temperature drop is about 200°C; this gives the maximum film surface temperature of 725°C.

The first wall surface temperature can be estimated by the turbulent heat transfer coefficient at the wall from the Colbrun correlation,[7] which is stated as:

$$\frac{h}{\kappa}\left[\frac{\mu^2}{\rho^2 g}\right]^{1/3} = 0.056\,Re^{0.2}\left(\frac{C_p\mu}{\kappa}\right)^{1/3} \qquad 6.8.2\text{-}61$$

The estimation of film temperature gradient based on the turbulent heat transfer coefficient predicted from the aforementioned equation and heat flux of 2.7×10^6 W/m^2 is about 10°C.

Although these preliminary calculations indicate that the film surface is cold enough for condensation to take place in a heavy ion driven IFE cavity and the first wall surface temperature is low, further analysis on the cavity clearing and liquid metal turbulent film heat transfer coefficient for condensation are needed to demonstrate that this concept is feasible.

Effect of Time-Dependent Cavity Pressure – Once an explosion occurs, some of the Pb film is vaporized and increases the cavity pressure. Under these circumstances, Pb may be pushed back into the cooling channels and the film will thin, slow down, and possibly become dry at the wall. In addition, the reactive impulse due to vaporized liquid and cavity shock waves may cause the same phenomenon, as well as disrupting the film surface. Here, the transient behavior of the film velocity and thickness are examined due to cavity pressure buildup. The effect of impulsive loading is beyond the scope of this work.

It is assumed that the pressure difference between the main coolant and the cavity can be expressed as:

$$\Delta P = P_{inlet} - 0.5\times10^6 \times (1 - e^{-t/3\tau}) \qquad (6.8.2\text{-}62)$$

where τ (~0.25 s) is the time interval between the explosions. This is a conservative estimate, since cavity clearing calculations estimate <0.1 MPa peak overpressure (see Section 6.8.2.5).

Figure 6.8.2-37 shows the assumed cavity pressure and pressure difference histories at the uppermost point of the cavity. The above equation does not attempt to simulate the real cavity pressure. (The cavity pressure at time of 0.25 seconds following the microexplosion falls below 1 mtorr.)

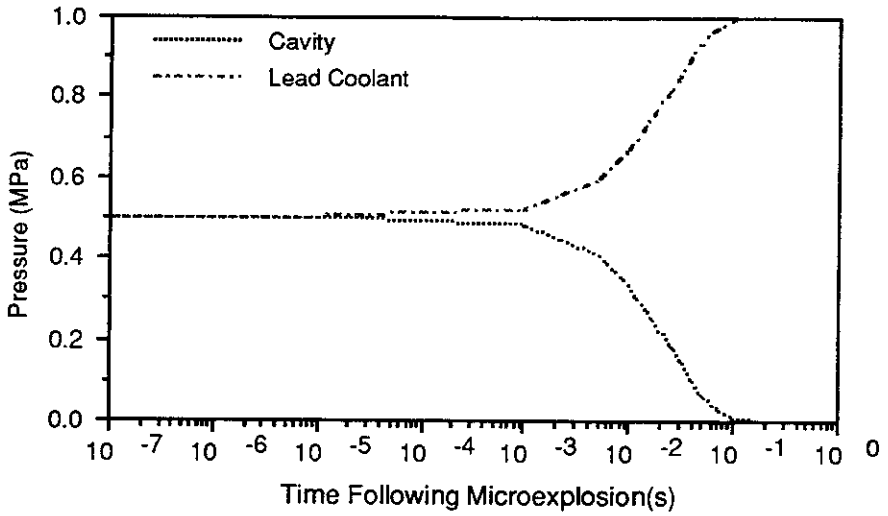

Figure 6.8.2-37. Cavity and Differential Pressure Histories at the Uppermost Point of the Cavity

The fluid equations include the transient Darcy's equation:

$$\rho\frac{\partial v}{\partial t} = -\frac{\partial P}{\partial y} + \frac{\mu}{\kappa}v \qquad (6.8.2\text{-}63)$$

and the transient film momentum equation:

$$\frac{\partial V}{\partial t} = -V\frac{\partial V}{\partial l} = g_c\cos(\theta) - \tau_D \qquad (6.8.2\text{-}64)$$

Example results of the ultimate film thickness and velocity histories following the cavity pressure build-up is shown in Figure 6.8.2-38. The case shown is for an initial jet velocity and film thickness of 20 m/s and 0.9 cm, respectively. The calculations indicate that the film velocity tends to decrease. If the initial jet velocity is not high enough, the film could even recede to the level where a dry wall occurs. For the case shown, the film approaches asymptotic (steady state) behavior at about 0.2 seconds following the cavity pressure build-up.

Flow Guiding Using Magnetic Forces – The analysis above indicates that a very thin film (<1 mm) is not obtainable on the inverted surface. (There is no limitation on the minimum film thickness on the vertical surface.) A possible mechanism to reduce the flow rate and film thickness while maintaining attachment is the use of guiding magnetic fields. Simple scaling analysis for achieving a thin film using a magnetic field was performed by Chao and Tillack.[8]

Summary – Although thin film flow provides attractive features for first wall protection, there are several technical issues remaining to be investigated to assess the feasibility of this concept. These include: (1) wetting characteristics of the lead on the SiC material, (2) flow on inverted surfaces, (3) problems in providing uniform coverage over large engineering structures, (4) flow past obstacles, such as beam penetrations,

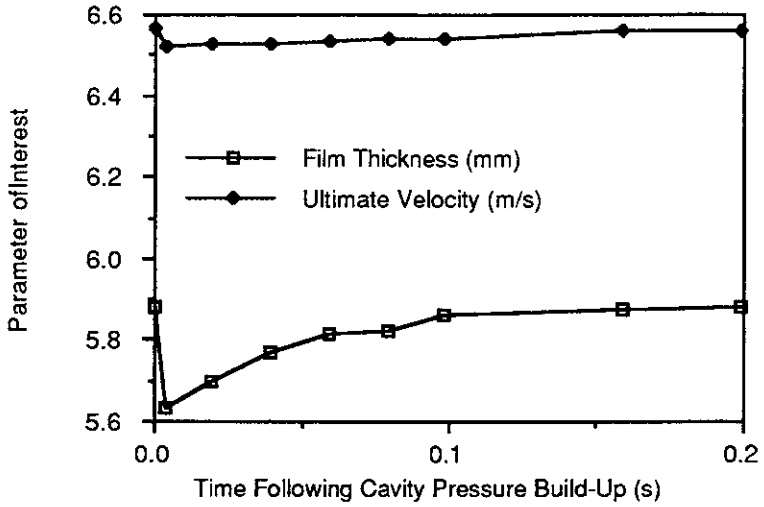

Figure 6.8.2-38. Ultimate Film Thickness and Film Velocity Histories Following the Cavity Pressure Build-Up

(5) stability of the film subjected to pressure impulses, (6) integrity of porous composite SiC material which is immersed in lead metal and subjected to a high radiation environment, and (7) consequences of dry spots.

References for 6.8.2.6

1. K. J. Chu and A. E. Duker, Statistical Characteristics of Thin, Wavy Films: Part II. Studies of the Substrate and its Wave Structure, A.I.Ch.E. Journal, Vol. 20, No. 4, 695 (1974).

2. Heishichiro Takahama and Seizo Kato, Longitudinal Flow Characteristics of Vertically Falling Liquid Films Without Concurrent Gas Flow, Int. J. Multiphase Flow, Vol. 6, pp. 203-215 (1980).

3. S. Ergun, Fluid Flow Through Packed Columns, Chemical Engineering Prog., 48, 89 (1952).

4. Richard H. French, Open-Channel Hydraulics, McGraw-Hill, New York, 1985.

5. G. Gimbutis, Heat Transfer for a Turbulent Falling Film, Proc. 5th Int. Heat Transfer Conf., Tokyo, Japan, Vol. 2, pp. 85-89 (1974).

6. Jon Lee, "Turbulent Film Condensation," A.I.Ch.E. Journal, p. 540, July 1964.

7. J. G. Collier, Convective Boiling and Condensation, Second edition, McGraw-Hill, New York, pp. 330-332, 1972.

8. T. C. H. Chao and M. Tillack, Evaluation of Alternatives to Avoid Dripping of Liquid Lead at the Upper End Cap in an IFE Reactor Cavity, UCLA-IFNT-8, October 1991.

6.8.2.7 Mechanical Response and Component Lifetime – Fatigue lifetime is a crucial issue in designing the first wall (FW) and blanket components of an IFE reactor. In order to assess the fatigue characteristics, a detailed structural response of the FW/B is required. Other factors such as the operating temperature, corrosive actions, etc., must also be investigated. A powerful method of analysis (e.g. Finite Element Method) should be used to extract the important fatigue data. However, some fatigue parameters, such as maximum stress level and frequency, can be reasonably estimated using analytical or finite difference methods. These methods can also be used to compare different design concepts, e.g., continuous FW versus segmented (modular) FW. In this part of the report, the rationale behind the structural material choice will be introduced. The mechanisms of mechanical loading of the wall will be identified. A discussion of specific results which enable the choice of the FW final configuration will be presented. Finally, an assessment of fatigue and lifetime of FW/B is discussed.

A SiC-SiC composite[1] manufactured by Societe Europeenne de Propulsion (SEP) is proposed as a reference structural material. This material reveals desired mechanical properties and oxidation resistance up to 1300°C. The basic mechanical properties of SEP 2D SiC-SiC composite are shown in Table 6.8.2-11 up to 1400°C. Preliminary tensile-tensile fatigue results at 100°C show that the material can survive 10^5 cycles at $\Delta\sigma \simeq 150$ MPa, with a residual ultimate tensile strength of ~90% of pre-test value. Toughness test results have also shown that SEP 2D SiC-SiC is ~50 times tougher than monolithic sintered SiC (in terms of energy absorbed at fracture).

Table 6.8.2-11 Properties of SEP-2D SiC-SiC*

Property	Units	Temperature		
		23°C	1000°C	1400°C
Density	g/cm^3	2.5	2.5	2.5
Porosity (Unirradiated)	%	10	10	10
Young's Modules (Tensile)	GPa	230	200	170
Poisson's Ratio				
ν_{12}		0.15	NA	NA
ν_{13}		0.4	NA	NA
Flexural Strength	MPa	300	400	280
Compressive Strength				
In Plane	MPa	580	480	300
Through the Thickness	MPa	420	380	250

* Adopted from Ref. 1.

The mechanical loading on the FW includes two basic mechanisms: (1) surface ablation momentum as a result of the early deposition of x-rays, and (2) time dependent pressure loading caused by evaporation from the protecting liquid lead film. Detailed description of the nature of the second mechanism is given in Section 6.8.2.4. The initial ablation momentum is introduced into the mechanical model as an initial velocity of the structure (using the principle of conservation of momentum). For a total impulse, I, uniformly distributed over the surface, the initial velocity, v_o, is given by:

$$v_o = \frac{1}{\rho h}\left(\frac{dI}{dA}\right) = \frac{1}{\rho A h} \qquad (6.8.2\text{-}65)$$

where A, ρ, and h are the total surface area, effective density, and thickness of the FW. Typical ablation momentum is found to be 3.17×10^3 N·s for the pellet parameters used in this study. A typical time variation of the local pressure (load) at FW is shown as a result of detailed hydrodynamics calculations, in Figure 6.8.2-39 for a base case of 5-m radius cavity.

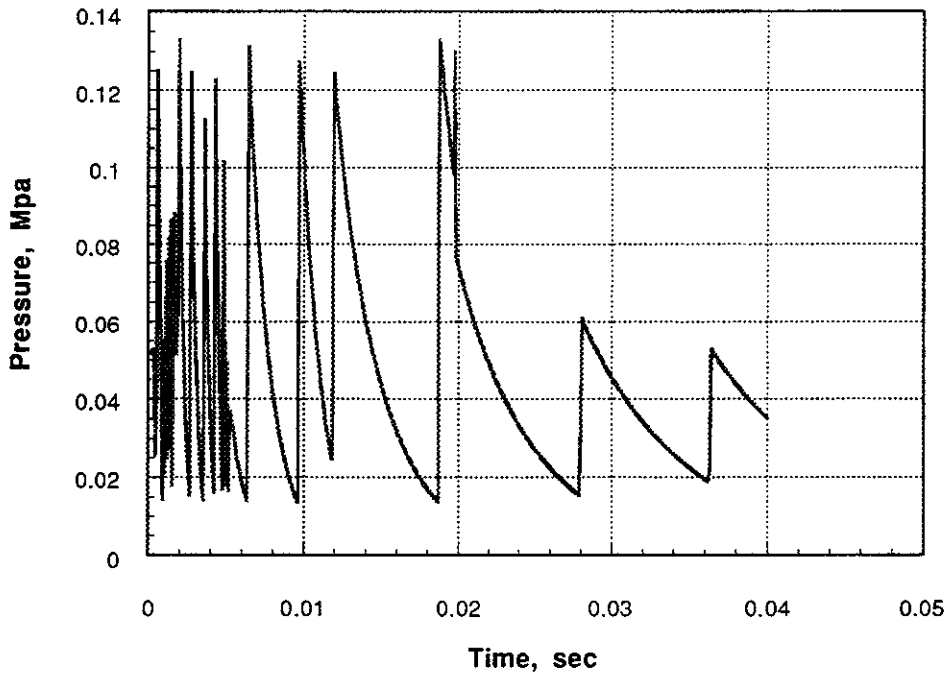

Figure 6.8.2-39. The History of the Pressure Loading on the First Wall Following the Microexplosion.

Spherical Shell Model – For a preliminary estimate of fatigue parameters of the cavity, a spherical shell model is considered (R = 5 m and h = 1 cm). The equation of motion is written as:[2]

$$\ddot{u} + \omega^2 u = \frac{P(t)}{\rho h} \qquad (6.8.2\text{-}66)$$

where u is the radial displacement, $\omega = \sqrt{\frac{2E}{\rho R^2}} = \frac{2\pi}{T}$ is the radial frequency of vibration, and P(t) is the time dependent pressure. For E = 200 GPa, the natural period, T, is ~2.5×10^{-3} sec. The hoop stress, σ, in the spherical shell is given by

$$\sigma(t) = E\frac{u(t)}{R}. \qquad (6.8.2\text{-}67)$$

The displacement and the radial velocity of the vibrating shell are shown in Figure 6.8.2-40. The hoop stress is shown in Figure 6.8.2-41. Notice that $u_{max} - u_{min}$ ~ 3.5 mm and $\Delta\sigma$ ~ 100–140 MPa at steady state. These values are not acceptable from the design point of view. Figure 6.8.2-42 shows the time dependent kinetic energy of the vibrating wall. Conclusions to be emphasized at this level of analysis are:

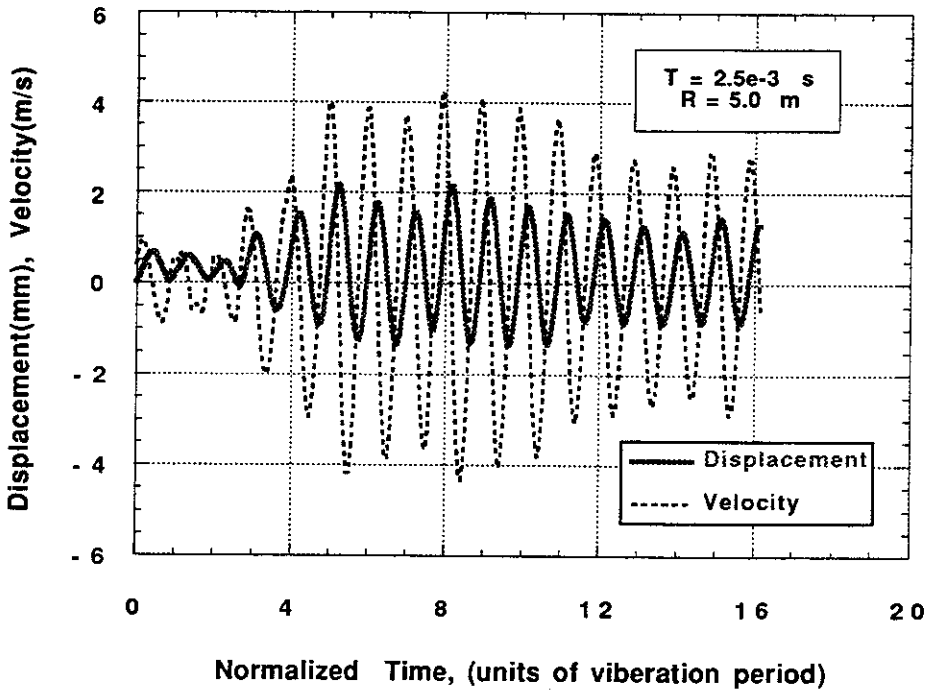

Figure 6.8.2-40. Instantaneous Velocity and Radial Displacement of the Continuous (Spherical Shell) First Wall.

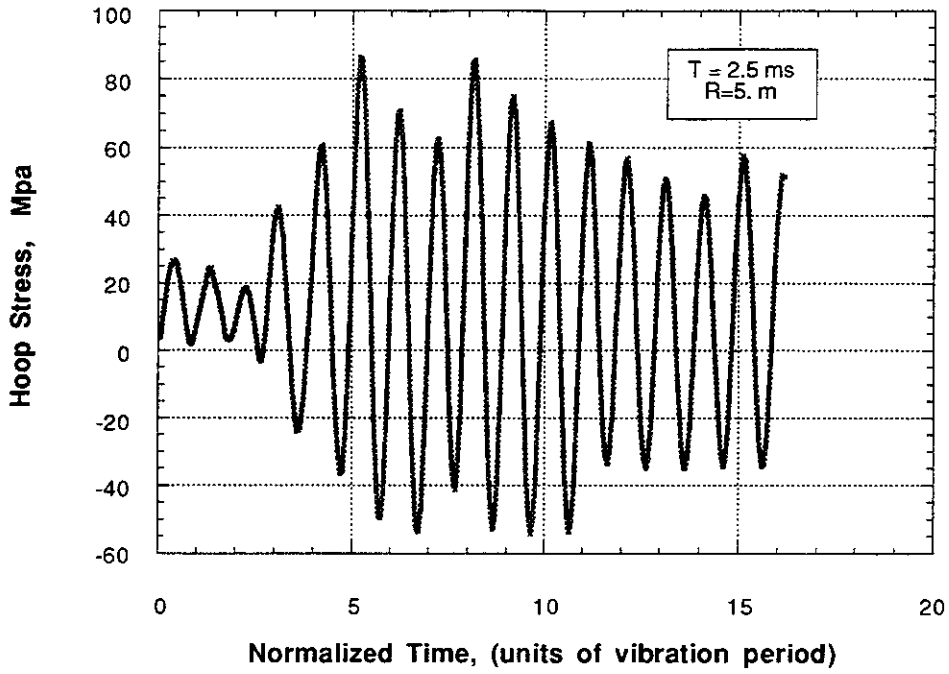

Figure 6.8.2-41. Hoop Stress History in the Continuous First Wall.

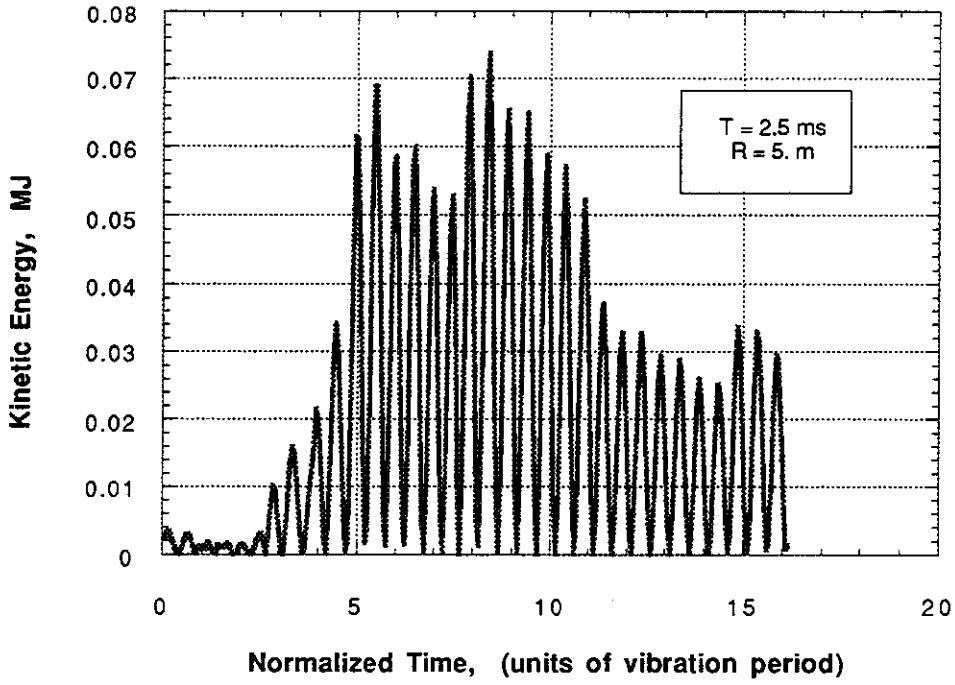

Figure 6.8.2-42. Kinetic Energy of the Vibrating Continuous First Wall.

(1) To avoid high stresses, segmentation of the FW is preferable. Integration of the FW with the blanket is also a reasonable design approach since it will constrain the vibration of the first wall.

(2) Because of the high velocity of vibration of the FW, the stability of the protecting film is an important issue.

(3) The maximum kinetic energy of the vibrating wall is ~0.07 MJ compared to pellet yield of ~655 MJ. This suggests that no damping mechanism is required.

First Wall Plate Model – According to the proposed configuration of the Prometheus-L reactor cavity, the FW is basically planar panels with an overall thickness of 6 cm. The panel can be viewed as a double-plate with both sides mechanically attached by perpendicular ribs, which separate the FW coolant channels. The panel size and method of support are determined by two factors: (1) the requirement that the maximum stress must be below its design limit, and (2) the maintenance scheme. Considering the mechanical support scheme for the FW, a planar panel can be modeled as a clamped plate subjected to ablation and pressure loading as a result of the pellet microexplosion. The effective plate thickness could be less than 6 cm due to the presence of coolant channels. Moreover, the presence of liquid lead provides very large inertial effects to the FW. Hence, the results underestimate the magnitude of the stress throughout the plate. The governing equation for the out-of-plane displacement u(x,y,t) is given by:[3]

$$P(t) = D_1 \frac{\partial^4 u}{\partial x^4} + 2D_3 \frac{\partial^4 u}{\partial x^2 \partial y^2} + D_2 \frac{\partial^4 u}{\partial y^4} + (\rho h) \frac{\partial^2 u}{\partial t^2} \qquad (6.8.2\text{-}68)$$

where $D_{1,2,3}$ are the orthotropic bending rigidity coefficients, (ρh) is the effective mass per unit area of the FW panels. Eq. 6.8.2-68 assumes that mid-plane symmetry exists. It also assumes zero transverse shear across the plate thickness. The orthotropic bending rigidity coefficients are given by:[3]

$$D_1 = \frac{E_1 h^3}{12(1 - \nu_{12}\nu_{21})}, \qquad D_2 = \frac{E_2 h^3}{12(1 - \nu_{12}\nu_{21})}$$

$$D_3 = D_{12} + 2D_{66}, \qquad D_{12} = \nu_{21} D_1,$$

$$D_{66} = \frac{G_{12} h^3}{12} \qquad (6.8.2\text{-}69)$$

where G_{12} is the shear modules in the plane of the panel, $E_{1,2}$ are the Young's moduli, and ν_{12}, ν_{21} are the Poisson's ratios.

The in-plane stresses can be recovered from the out-of-plane displacement as follows:

$$\sigma_x = (Q_{11}k_x + Q_{12}k_y)z ,$$

$$\sigma_y = (Q_{12}k_x + Q_{22}k_y)z ,$$

$$\sigma_{xy} = 2Q_{66}k_{xy}\, z \qquad (6.8.2\text{-}70)$$

where Q_{ij} = stiffness coefficients of the composite material, z is the distance measured from the mid-plane (as shown in Figure 6.8.2-43) and k_x, k_y, and k_{xy} are given by:

$$k_x = - \partial^2 u/\partial x^2 , \qquad k_y = - \partial^2 u/\partial y^2 ,$$

$$k_{xy} = - \partial^2 u/\partial x \partial y \qquad (6.8.2\text{-}71)$$

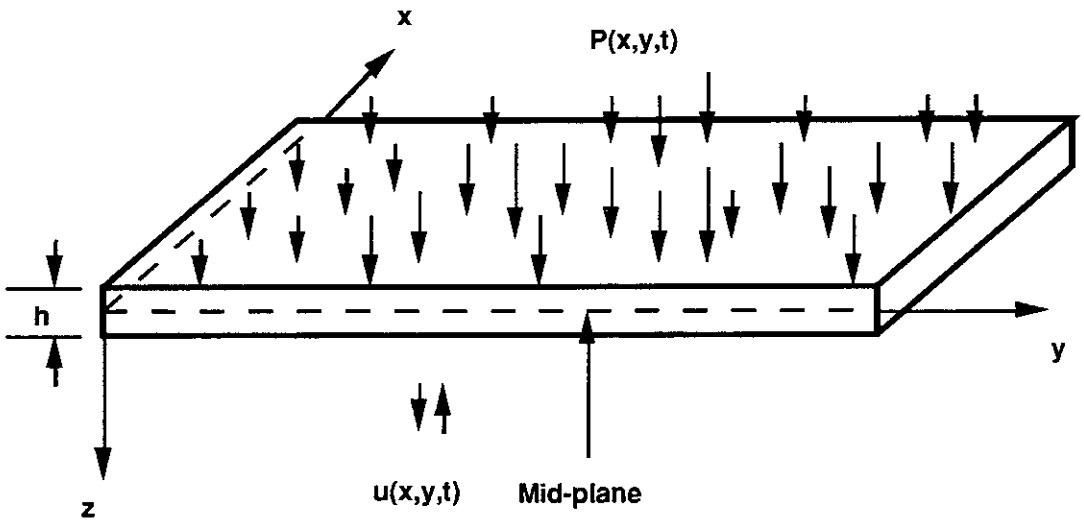

Figure 6.8.2-43 Schematic of Mechanical Loading of the FW Panels.

The equation of motion is solved using the finite difference technique.[4] The solution is formulated for different mesh size along x and y axis. The resulting matrix equation is written as :

$$A\, u = b \qquad (6.8.2\text{-}72)$$

where A is constant coefficient matrix, u is the nodal displacement vector, and b is the time dependent load vector. At each time step, the load vector is evaluated in terms of the instantaneous local pressure and the last time step values of the displacement vector. The matrix A is NxN where N is the total number of nodal points. At each node, the initial displacement is zero and, by using Eq. 6.8.2-65, the initial velocity is determined to be 0.03 m/s all over the plate. At clamped edges, the displacement and its first spatial derivative are set equal to zero at all times. Upon enforcing these boundary conditions, a Guassian Elimination Technique[5] is used to solve the matrix Eq. 6.8.2-72 at each time step. The stresses are recovered from the solution for the displacement using Eqs. 6.8.2-70 and 6.8.2-71.

The results for a clamped plate 1m x 1.5m are shown in Figures 6.8.2-44 through 6.8.2-46. The fundamental frequency of vibration was found to be ~800 Hz. It is observed that the resonance between the mechanical response of the FW panels and the pressure loading is of small probability since the frequency with which the pressure changes (Figure 6.8.2-39) is variable over the time between two microexplosions. Maximum displacement of about 0.1 mm is determined, which can be allowable. The maximum stresses always occur at the clamped edge (Figure 6.8.2-46). The implications on the fatigue and failure of the structure will be explained through the following discussion.

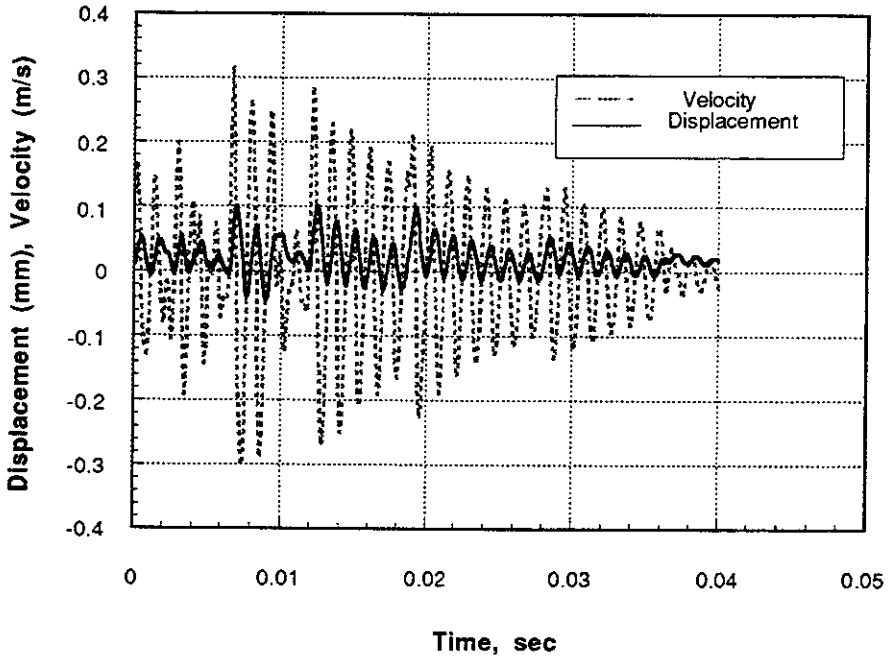

Figure 6.8.2-44. Instantaneous Velocity and Displacement at Center of First Wall Plate (1m x 1.5m)

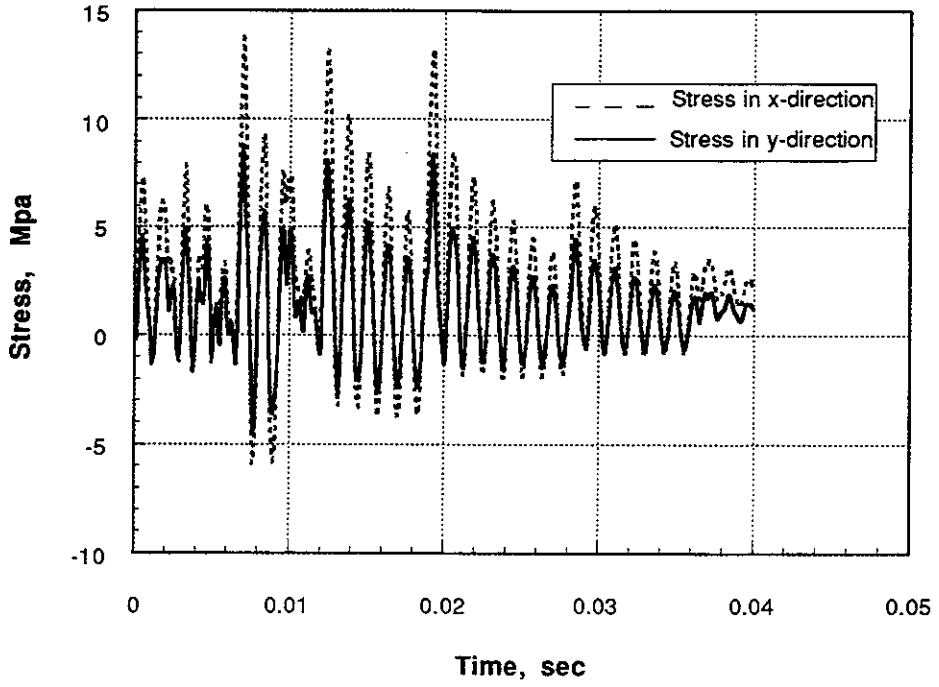

Figure 6.8.2-45. The History of Stresses at Center of FW Plate (1m x 1.5m)

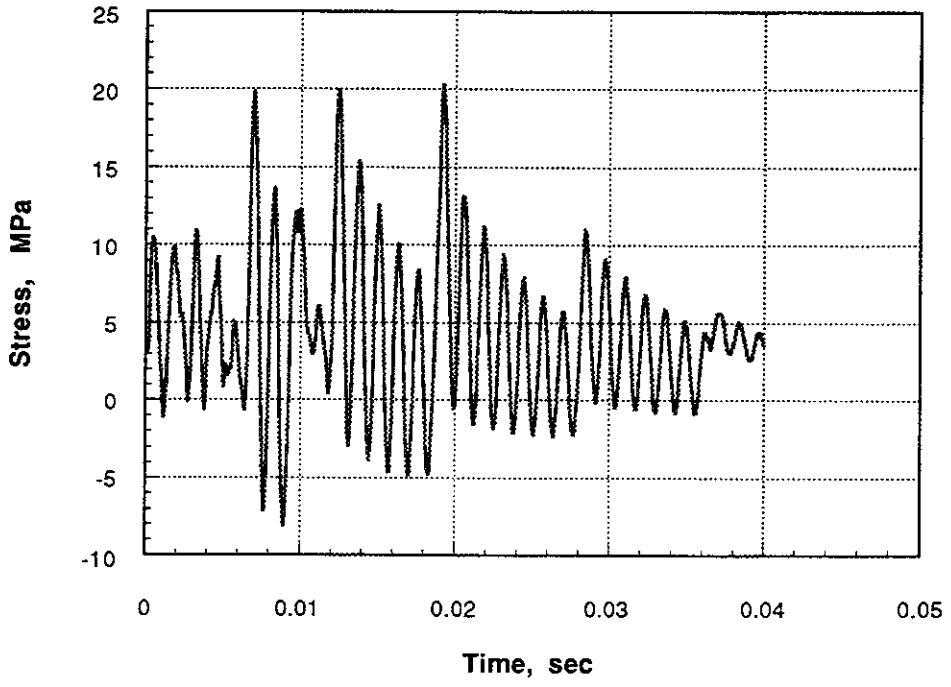

Figure 6.8.2-46. The History of Stresses at Clamped Edge of FW Plate (1m x 1.5m)

First Wall Fatigue Damage – The process of fatigue damage and failure in composites is highly complicated. As a result, standard methods have not been established to define design criteria for fatigue design with composite materials. However, some designers assume the classical method, S-N diagrams, to apply.[6] Others[7] have presented a systematic conceptual scheme for evaluation of fatigue performance of composites based on certain damage mechanism maps, called fatigue-life diagrams. In the later approach, failure is based on a strain criterion; that is, for a composite material, the fatigue limit is defined as the strain corresponding to the boundary between the non-propagating matrix cracks and the propagating matrix cracks at 10^6 cycles. However, the fatigue-life diagrams have been established only for a limited number of materials.

Figure 6.8.2-47 shows the stress-strain diagram for SEP 2D SiC/SiC composite material[1] in which the fatigue tested material is compared to the pre-test material. For 10^6 cycles at 100 MPa, the fatigue tested material shows a very promising behavior. It can be noted that the rupture characteristics were maintained. Only the modules at the origin dropped slightly by ~18%. The maximum stress (Figure 6.8.2-46) in the present

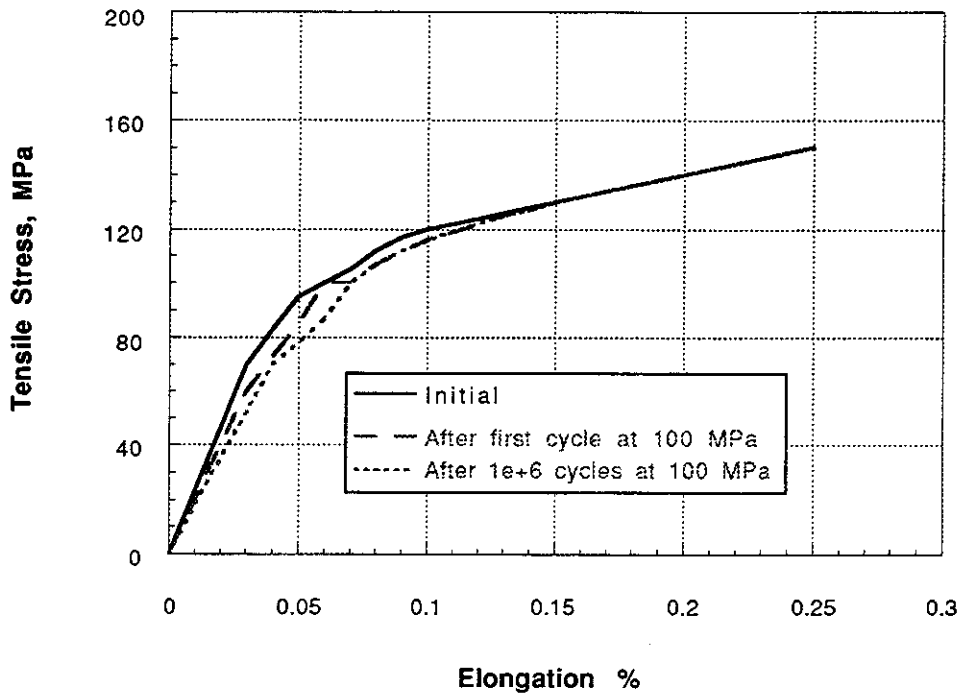

Figure 6.8.2-47. The Stress-Strain Diagram for SEP 2D SiC/SiC Composite (Fatigue Tested vs. Virgin Material). Data from Reference 1.

design is observed to be ~20 MPa which is far below 100 MPa. This means that, as a first approximation, the FW structure can survive at least 10^6 cycles at the given stress conditions. It is concluded here that the lifetime of the FW structure is not controlled by fatigue damage, but rather by radiation effects on the structural properties of the SiC-SiC composite material.

References for 6.8.2.7

1. A. Lacombe and C. Bannet, "Ceramic Matrix Composites, Key Materials for Future Space Plane Technologies." AIAA Second International Aerospace Planes Conference, 29-31 October 1990, Orlando, FL, USA.

2. L. A. Gleen and D. A. Young, "Dynamic Loading of the Structural Wall in a Lithium-Fall Fusion Reactor.", Nucl. Eng. Design 54, 1-16 (1979).

3. J. R. Vinson and R. L. Sierakowski, "The Behavior of Structures Composed of Composite Materials.", Kluwer Academic Publishers, 1987.

4. S. P. Timoshinko and J. N. Goodier, "Theory of Elasticity.", 3rd Ed., McGraw-Hill Book Co., 1987.

5. C.F. Gerald and Patrick O. Wheatley, "Applied Numerical Analysis.", 3rd Ed., Adison-Wesley Pub. Co., 1984.

6. International Encyclopedia of Composites, Vol. 2. Editor: Stuart M. Lee. 1990.

7. Ramesh Talreja, "Fatigue of Composite Materials.", Technomic Pub. Co., 1987.

6.8.2.8 Component Lifetime Assessment - Determination of the lifetimes for various structural components is highly dependent on uncertainties in structural modeling and in the materials data base. However, a first-order assessment of first wall and blanket (FW/B) lifetimes is possible if a number of assumptions are made. For the purposes of this analysis of FW/B component lifetimes, the effects of the following factors were analyzed.

(1) Mechanical loading fatigue damage.
(2) Compatibility with Pb and He coolants.
(3) Radiation effects.

Fatigue Damage - As outlined in the previous section, fatigue damage of the FW should be carefully considered. A complicated spectrum of cyclic stresses results from the impact of the rapid pressure and impulse loading on the first wall. The edge of the FW plates are identified as critical because of the constraint conditions imposed. It is seen from Figure 6.8.2-46 that the maximum in-plane stress is on the order of 20 MPa and that its frequency is approximately 3-4 times per shot. Many other smaller amplitude stress cycles can also be seen, but their effects are neglected at the present time. The large amplitude stress cycles are not fully reversed, but they range approximately between +20 MPa to -5 MPa. Prometheus-L approximate parameters were used for the spectral effects of cycling.

Stress Cycle	=	+20 MPa to -5 MPa
Frequency	=	5.6 x 4 = 22.4 Hz
No. of Cycles/Year	=	7×10^8

The approximate stress characteristics diagram is shown in Figure 6.8.2-48.

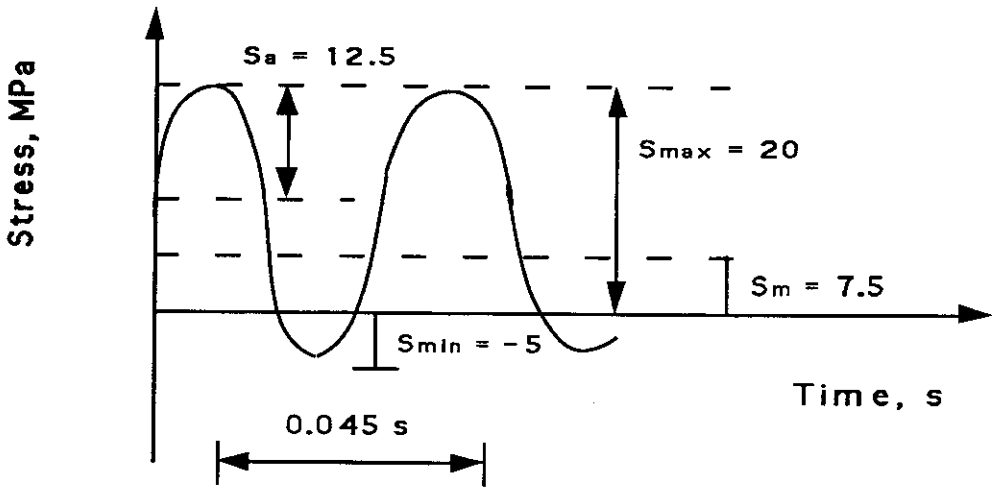

Figure 6.8.2-48. First Wall Stress Characteristics Diagram

Tensile data on SEP 2D SiC/SiC composites indicate that the effective ultimate strength is on the order of 160 MPa. However, significant deviations from linear stress-strain behavior are deserved at about 80-100 MPa. Such behavior is indicative of matrix micro-cracking. For lack of extensive fatigue experience with ceramic matrix composites, we follow a conservative approach was used such as in low ductility metallic structures (i.e., high strength steels). A fatigue ratio in the range of 0.35 to 0.5 is obtained for all high strength, low-ductility materials(1).

The S-N diagram will be constructed on the basis of the most conservative of the following for the fatigue endurance limit, S_f,

Modified Goodman, $$\frac{S_a}{S_f} + \frac{S_m}{S_u} = 1$$

Gerber, $$\frac{S_a}{S_f} + \left(\frac{S_m}{S_u}\right)^2 = 1$$

Morrow, $$\frac{S_a}{S_f} + \frac{S_m}{\sigma_u} = 1$$

In these equations, S_a is the alternating stress, S_f the endurance limit, S_m is the mean stress, σ_f is a fracture stress, and σ_u is the ultimate stress. We will not use the Soderberg line because it is more appropriate for ductile metals with a definite yield point. The approximate S-t diagram gives the following:

$Sm = 7.5$ MPa

and the SEP data shows that:

$S_u \simeq \sigma_f \simeq 100$ MPa

Following the Morrow (or Goodman) analysis, we get

$$\frac{S_a}{40} + \frac{7.5}{100} = 1 \qquad \therefore S_a = 37 \text{ MPa}$$

Since the allowed S_a is larger than 12.5 MPa, the structure is safe as far as fatigue life is concerned. A safety factor of 3 indicates a high degree of structural reliability. It accounts for fatigue data uncertainties, as well as any stress concentrations around notches and stress raisers. The S-N diagram is shown in Figure 6.8.2-49.

We conclude from our analysis that the fatigue endurance limit of the SiC/SiC composite will not be exceeded. The lifetime will, therefore, be determined by other issues, such as coolant compatibility and radiation effects.

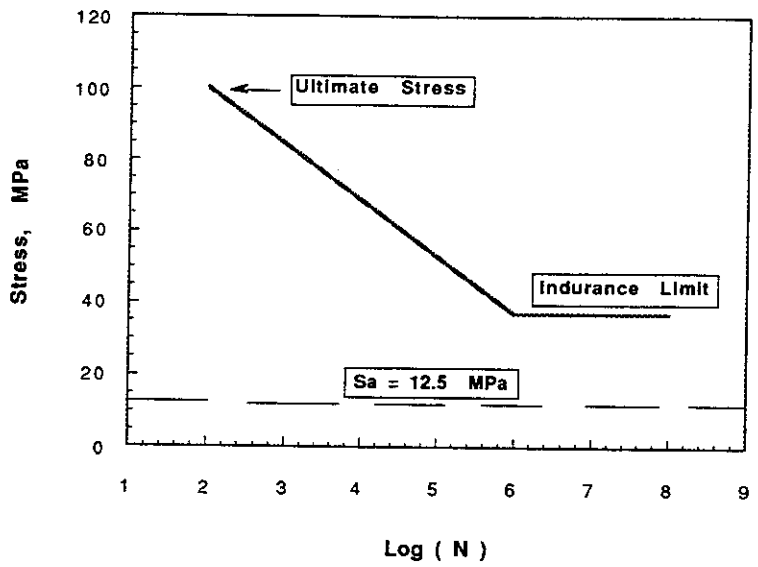

Figure 6.8.2-49. S-N Fatigue Design Curve for the SiC First Wall

Coolant Compatibility - Two main coolants are used in the FW/B systems of Prometheus. Thermodynamic data on the compatibility of Pb with SiC is very scarce, and the indications point to a thermodynamically compatible system. However, even though helium is an inert gas, it will contain low level impurities of O_2 and H_2O. Since the fiber-matrix interface will be C, BC_4 or BN at the present time, we must also investigate the effects of oxygen impurities on the chemical stability of the interface.

When SiC is exposed to a highly oxidizing atmosphere, such as air, a dense SiO_2 layer forms on the surface and further oxidation is retarded. Because of this passivation, SiC exhibits excellent oxidation resistance at high temperatures. However, when the supply of oxygen is not sufficient (in reducing or inert atmospheres), the protective SiO_2 layer cannot form and weight loss occurs by decomposition or active oxidation of the SiC. Such corrosion can significantly affect the strength of the SiC by introducing flaws to the surface or reducing the load-bearing cross section.

Under fusion conditions, the average temperature is generally in the range 773 and 1273 K, and the impurities in the helium coolant average between 100 and 1000 ppm. For these conditions, we have a typical hot corrosion process. The growth of an oxide can be compared with current flow around a circuit containing an electrolytic cell. It will include both electronic and ionic parts. The ionic current produces two effects:

(a) The ionization of metal atoms, Me = M(Z+) + z electrons
(b) The ionization of oxygen atoms, O + 2 electrons = O(2-)

The computer code CET (Chemical Equilibrium Thermodynamic) Code developed by NASA was used in the present study to calculate the equilibrium compositions of the system. This procedure is based on minimization of the total free energy of the system, which was originally developed by Gorden and McBride and revised by Zeleznik.[2]

The total Gibbs free energy of a system is given by the equation:

$$G=\sum_{i=1}^{n} n_i g_i=\sum_{i=1}^{n} n_i\left(g_i^0 + RT \ln a_i\right) \qquad (1)$$

(6.8.2-73)

where G is the total Gibbs free energy of a system, R is the ideal gas constant, T is the thermodynamic temperature, n_i is the moles of chemical species "i", and a_1 is the activity of species "i".

Calculations with the CET program were performed for a wide range of conditions which are relevant to the study. The stability of SiC and possible interfaces such as BN, B_4C, and C was also investigated in the temperature range 773 - 1273 K. The conditions are summarized in Table 6.8.2-12.

Table 6.8.2-12 Conditions for Chemical Compatibility of SiC/SiC Composites with Helium

Materials	SiC, BN, C
Impurity Levels	100-1000 ppm
Impurity Type	H_2O, O_2
Temperature Range	773-1273 K

Hydrogen, oxygen and water moisture are expected to be contained in the main coolant, helium.

Silicon carbide will chemically react with O_2, H_2O, and H_2, according to the following reactions:

$SiC(s) + O_2(g) = SiO(g) + CO(g)$
$2SiC(s) + 3O_2(g) = SiO(g) + CO_2(g)$
$2SiC(s) + O_2(g) = SiO(g) + C$
$SiC(s) + O_2(g) = Si + CO_2(g)$
$2SiC(s) + O_2(g) = Si + CO(g)$
$SiC(s) + 2H_2O(v) = SiC(g) + CO(g) + 2H_2(g)$
$SiO_2(s)(\text{Protective layer}) + H_2(g) = SiO(g) + H_2O(v)$

Relevant reactions for forming a protective layer are given below:

$$SiC(s) + 2O_2(g) = SiO_2(s) + CO_2(g)$$
$$2SiC(s) + 3O_2(g) = SiO_2(s) + CO(g)$$
$$SiC(s) + O_2(g) = SiO_2(s) + C(s)$$

For the C and BN fibers we have the next relevant reactions:

$$C(s) + O_2(g) = CO_2(g)$$
$$2C(s) + O_2(g) = 2CO(g)$$
$$2BN(s) + 2O_2(g) = 2BO_2(g) + N_2$$
$$2BN(s) + 3H_2O(v) = B_2O_3(g) + 2NH_3$$

The kinetics of these reactions can be affected by the formation of a protective layer of SiO_2 at high partial-pressure of O_2 such that SiC is stable in many corrosive environments.

The molar fractions of gases in equilibrium with SiC in contact with the helium coolant containing 100 ppm O_2 to 1000 ppm O_2 are shown in Figures 6.8.2-50 through 6.8.2-53. In these cases, the primary gaseous products were found to be CO and CO_2 and small amounts of SiO and SiO_2 in equilibrium with the condensed phase of SiO_2 protective layer. Figures 6.8.2-50 and 6.8.2-51 show the molar fraction of the dominant gaseous species, while Figures 6.8.2-52 and 6.8.2-53 give the molar fraction of the condensed species SiO_2 and graphite as function of temperature. The dominance of CO and CO_2 gaseous oxides indicate that the surface of SiC tubes and structures in the blanket will be quickly enriched with Si and, hence, will form a protective SiO_2 coating.

The effects of water moisture on the formation of gaseous oxides are illustrated in Figures 6.8.2-54 through 6.8.2-57. In this case, additional hydro-carbons (CH_3 and CH_4) form. However, the same behavior is exhibited where the protective SiO_2 layer forms.

The following conclusions can be made from the studies:

(1) The dominant gaseous species which form in equilibrium with SiC are CO, CO_2, SiO, and SiO_2 where the helium coolant contains O_2 impurities.
(2) When water moisture is trapped in the helium coolant, additional hydro-carbons (CH_3 and CH_4) will form.
(3) In all cases considered, graphite and SiO_2 will exist in the solid phase. Thus, further hot corrosion of the SiC surface will halt.

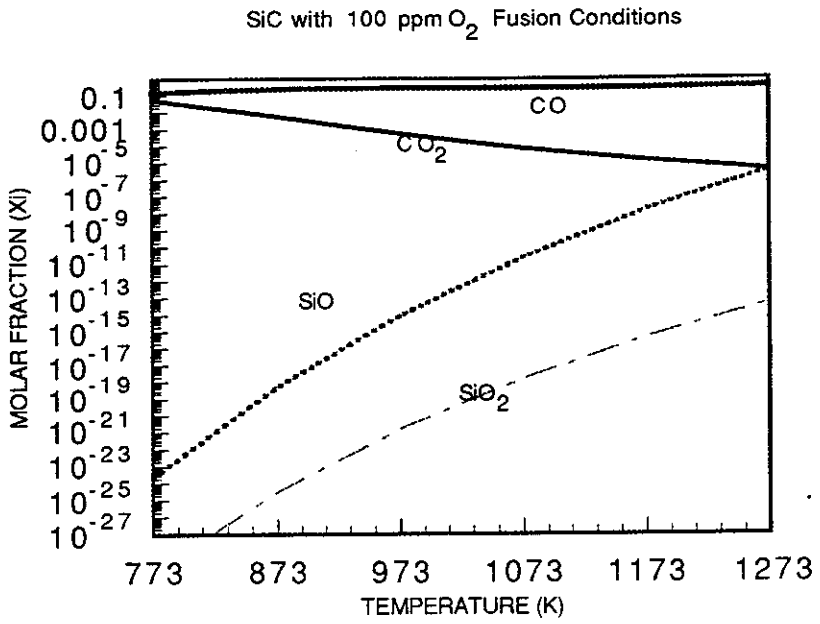

Figure 6.8.2-50. Molar Fractions of Main Chemical Species in SiC with 100 ppm O_2 Impurity Level

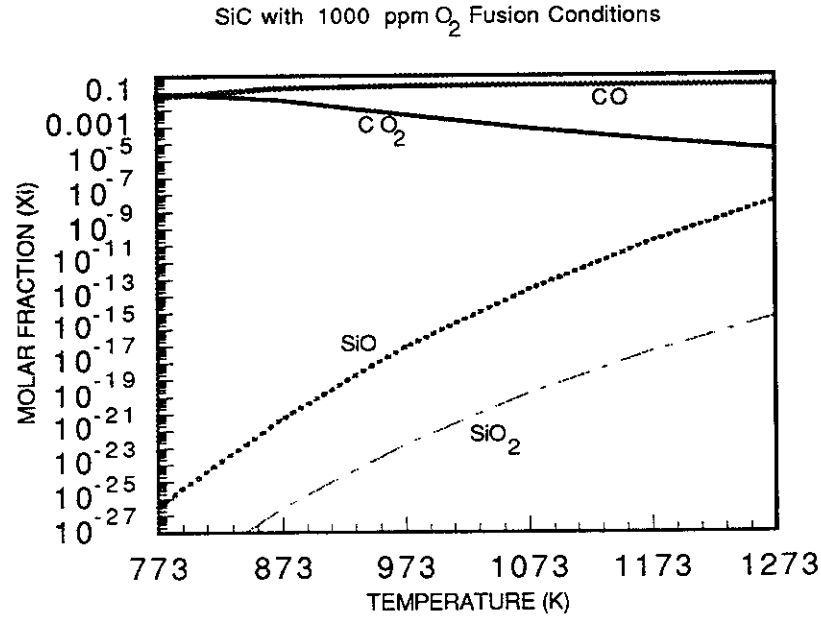

Figure 6.8.2-51. Molar Fractions of Main Chemical Species in SiC with 1000 ppm O_2 Impurity Level

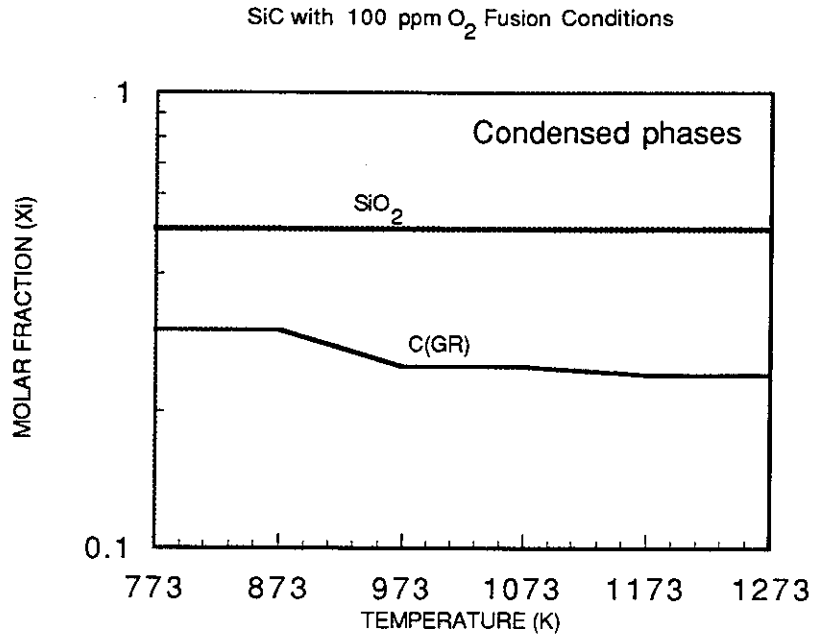

Figure 6.8.2-52. Molar Fractions of Solid (Condensed) Phases in SiC with 100 ppm O_2 Impurity Level

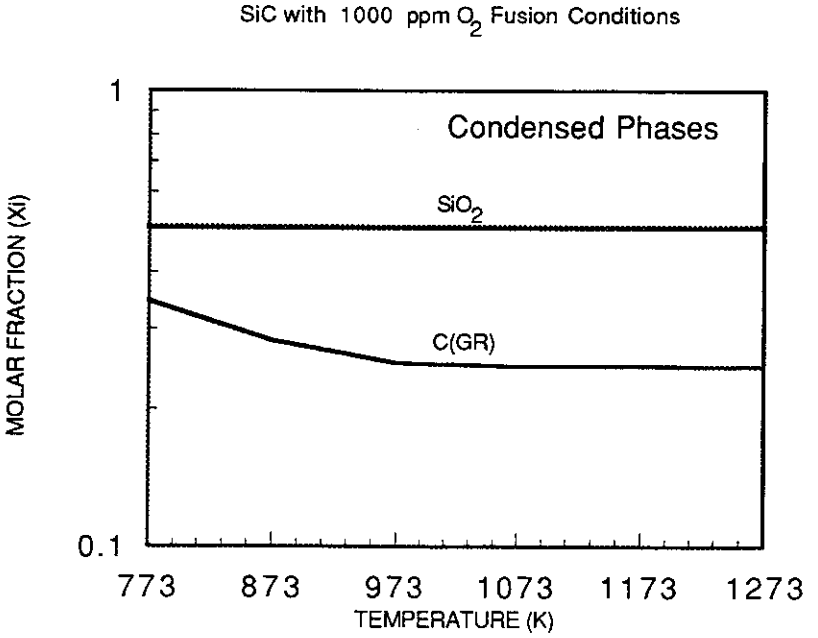

Figure 6.8.2-53. Molar Fractions of Solid (Condensed) Phases in SiC with 1000 ppm O_2 Impurity Level

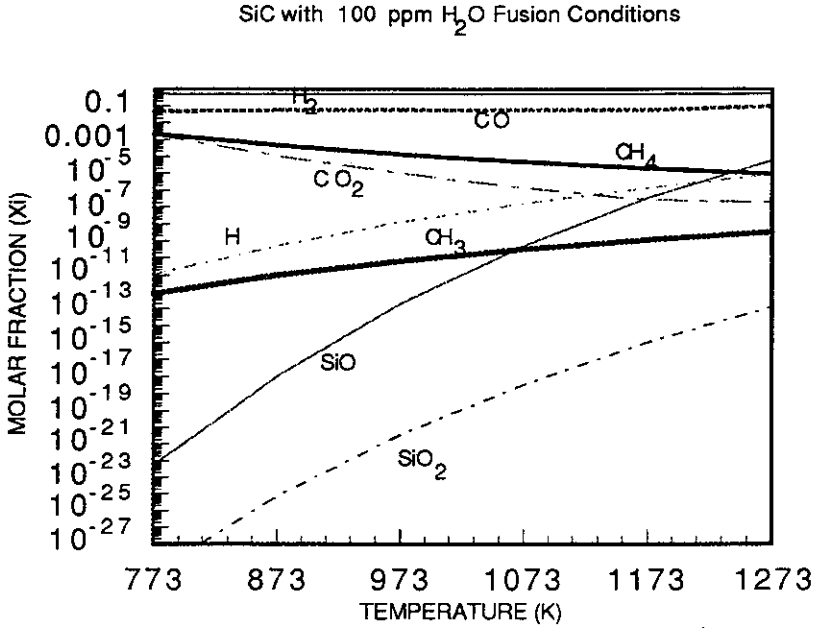

Figure 6.8.2-54. Molar Fractions of Main Chemical Species in SiC with 100 ppm H_2O Impurity Level

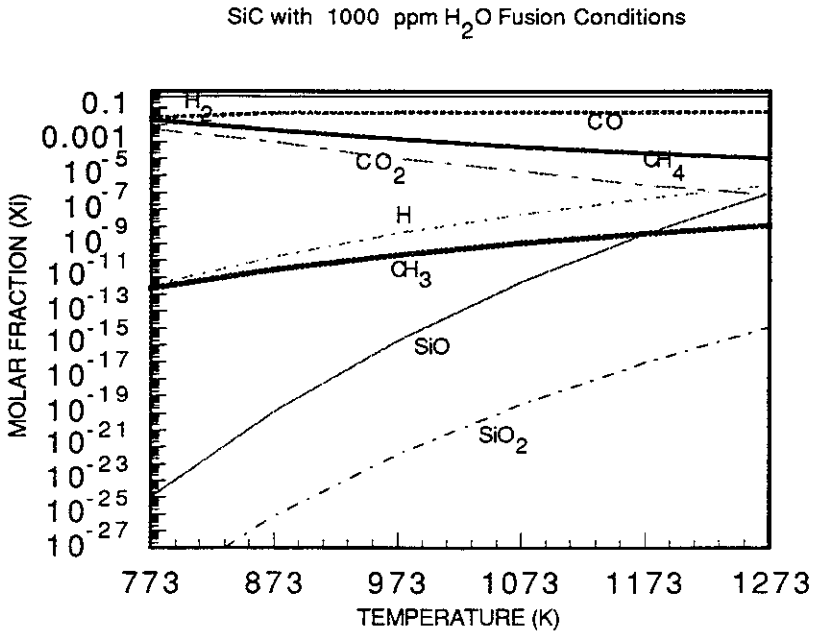

Figure 6.8.2-55. Molar Fractions of Main Chemical Species in SiC with 1000 ppm H_2O Impurity Level

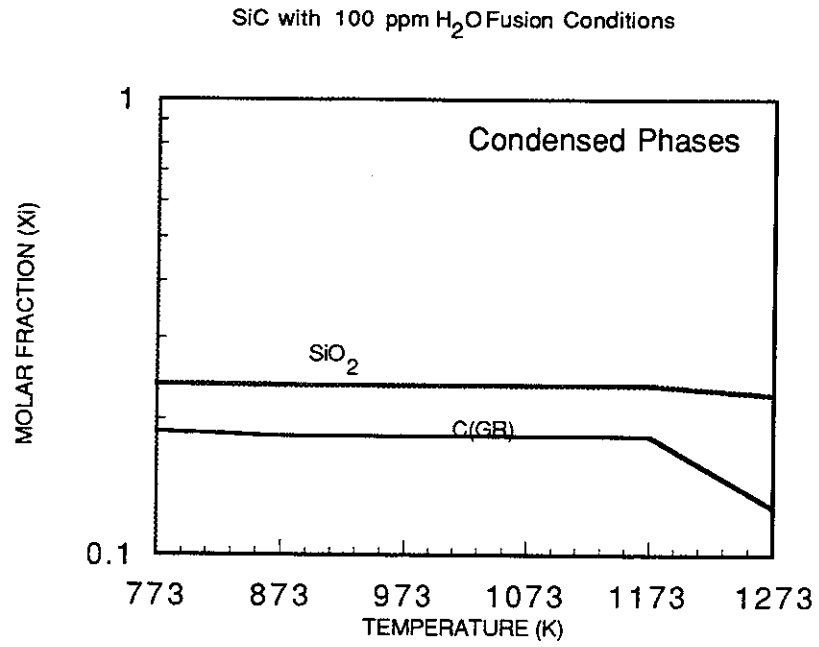

Figure 6.8.2-56. Molar Fractions of Condensed (Solid) Phases in SiC with 100 ppm H_2O Impurity Level

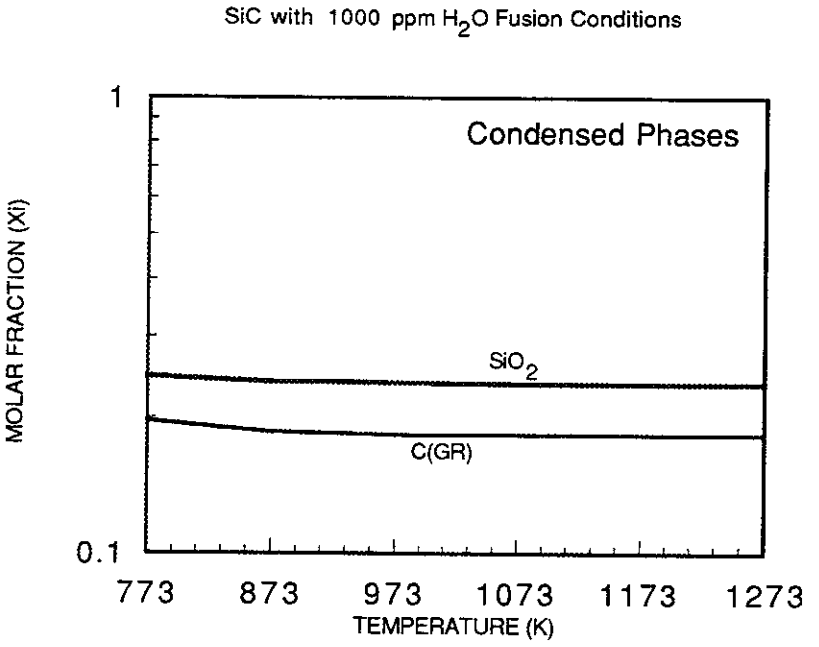

Figure 6.8.2-57. Molar Fractions of Condensed (Solid) Phases in SiC with 1000 ppm H_2O Impurity Level

Oxidation of the interface between the fibers and the matrix can be a serious issue because it may lead to strength degradation. Our detailed studies of the chemical stability of C and BN interfaces indicate that these two types of interfaces will not be stable under the conditions outlined in Table 6.8.2-12. A search for an appropriate low-activation and chemically stable fiber/matrix interface is, therefore, identified as an important area which needs further development.

The main conclusion we draw from this work is that SiC will be chemically stable in the coolant environment of the blanket. Care, however, must be taken to determine the stability of the fiber/matrix interface.

Radiation Effects - The strong directional bonding and the mass difference between Si and C atoms render the crystalline form of β-SiC exceptional radiation resistance characteristics. Recent Molecular Dynamics (MD) studies[3] show that Replacement Collision Sequences (RCS's) are improbable and that the displacement of C atoms is much easier than Si. MD computer simulations[3] show the average threshold displacement cascade differs substantially from that of the matrix. It is also observed that energetic Si PKA's displace multiple C atoms which end up on <111> planes. Experimental observations at temperatures below 1000°C corroborate this conclusion.[15] Vacancies and He atoms exhibit considerable mobility above 1000°C. These fundamental considerations may explain some of the observed features of SiC dimensional changes as function of temperature and fluence.[4-7]

Price[4] observed Frank-type loops on {111} planes which may be C-rich. Below 1000°C, point defects tend to form loops on {111} planes and swelling is, therefore, expected to saturate. For example, Harrison and Correli[8] observed large loops (10-200 nm) in β-SiC after neutron irradiation to fluence of 1.8×10^{23} cm^{-2}. At temperatures above 1000°C, cavities form and swelling does not saturate. The presence of helium results in further increases in the swelling rate by the known gas-driven swelling mechanism. Swelling of β-SiC in temperature range 625-1500°C and at neutron fluence (E>0.18 MeV) of 1.2×10^{22} cm^{-2} [Ref4] is represented by two separate polynomials with two different sets of coefficients below and above 1000°C, respectively. The coefficients and the general swelling behavior as a function of temperature is shown in Figure 6.8.2-58. Additional helium will drive swelling to higher values, particularly at temperatures above 1200°C.[20] The limited accumulated evidence from radiation effects data indicate that the upper temperature limit for use of SiC in structure design is in the range of 900-1000°C.

Figure 6.8.1-9 shows the neutron spectrum for Prometheus-L for a neutron source, $S_0 = 9.83 \times 10^{20}$ n/s. Since the swelling data is correlated to the fast neutron flux (E>0.18 MeV), an estimate of the swelling rates in the blanket and first wall can be made by finding the flux for $E \geq 0.2$ MeV. The high energy neutron spectrum is also shown in Figure 6.8.1-11. Table 6.8.2-13 shows the relevant neutron flux for design purposes.

Table 6.8.2-13 Total Neutron Flux $\Phi x 10^{-15}$ ($n/cm^2/s$) ($E \geq 0.2$ MeV)

	Prometheus-L	Prometheus-HI
FW	1.97	2.27
B	1.37	1.58

SiC/SiC composites manufactured by the CVI process will contain porosity, ranging from 10-30%. On the basis of the limited swelling data shown in Figure 6.8.2-58, the volumetric swelling of the first wall and blanket are shown in Figures 6.8.2-59 and 6.8.2-60. The design limit will be set here on the basis of a maximum volumetric deformation of 5-6% (i.e., accumulated inelastic linear strains of ~2%). It can be concluded here that the lifetime of first wall structure is estimated at 2.5 to 7.7 years for Prometheus-L and 2.1 to 6.7 years for Prometheus-H. The blanket lifetime is likewise estimated at 3.5 to 11 years for Prometheus-L and at 3 to 9.6 years for Prometheus-H.

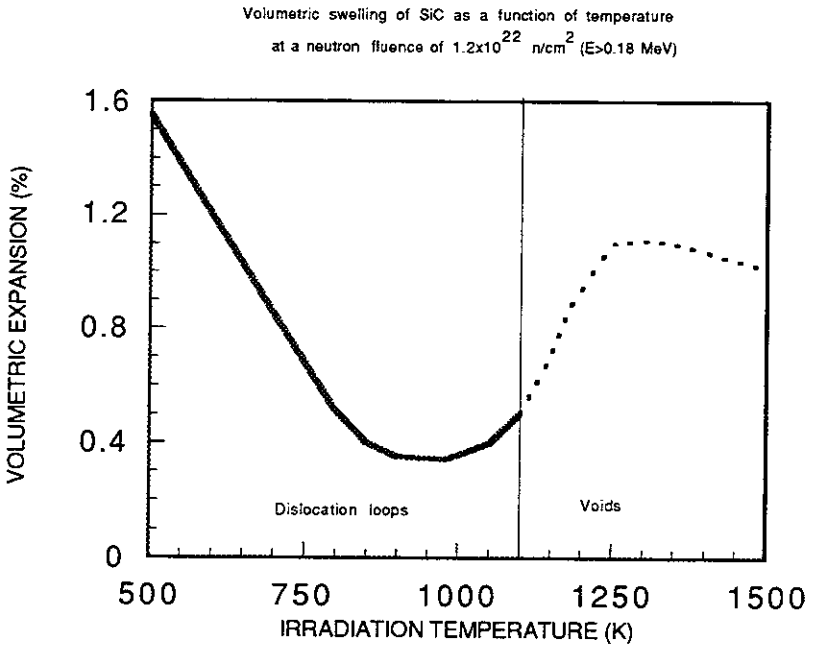

Figure 6.8.2-58. Volumetric Swelling of SiC as a Function of Temperature at a Neutron Fluence of 1.2×10^{22} ncm^{-2} ($E > 0.14$ MeV)

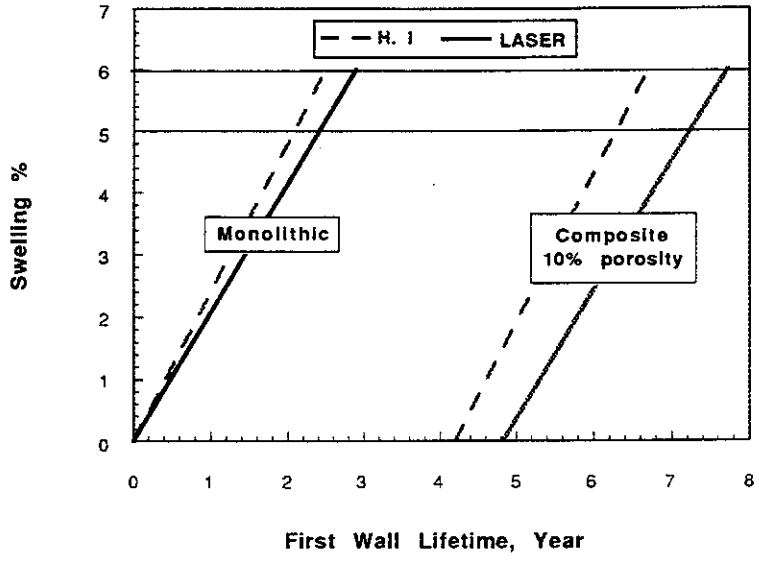

Figure 6.8.2-59. Estimated Total Volumetric Swelling for the First Wall Structure

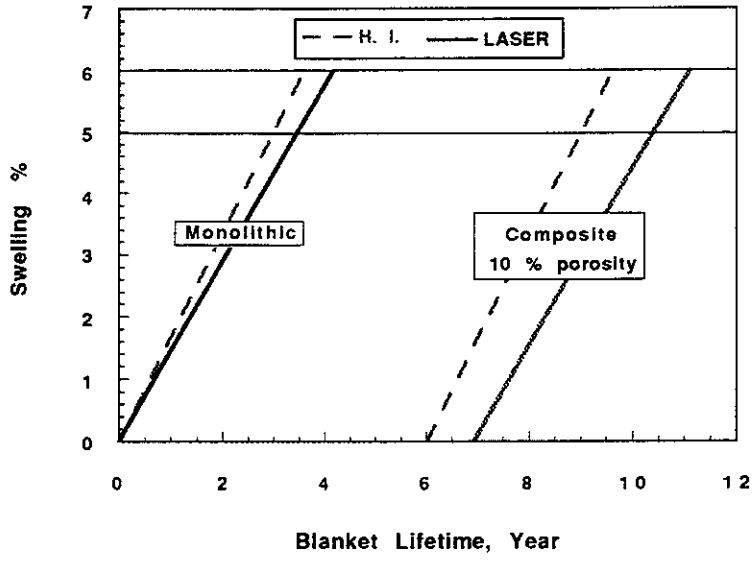

Figure 6.8.2-60. Estimated Total Swelling for the SiC Blanket Structure

References for 6.8.2.8

1. H. O. Fuchs & A. I. Stephens, Metal Fatigue in Engineering, John Wiley & Sons, N. Y., 1980

2. S. Gorden & B. J. McBride, "Computer Program for Calculation of Complex Chemical Equilibrium Compositions, Rocket gas and Reflect Shock", NASA Lewis Research Scientific and Technical Information Office, Report # NASA-SP-273, March 1973

3. A. Elazab and N. M. Ghoniem, Proc. of Fifth Int. Conf. on Fusion Reactor Materials, Clearwater, FL, November 1991

4. R. J. Price, J. Nuclear. Materials, 46, p. 268, (1973).

5. R. Blackstone and E. H. Voice, J. Nuclear. Materials, 39, p. 319 (1971).

6. A.M. Carey, F. J. Pineau, C. W. Lee, and J. C. Corelli, J. Nuclear. Materials, 103 & 104, p. 789 (1981).

7. K. Hojou and K. Izui, J. Nuclear. Materials, 160, p. 334, (1988).

8. S. D. Harrison and J. C. Corelli, J. Nuclear. Materials, 122 & 123, p. 833, (1984)